

Final Draft
of the original manuscript:

Liu, J.; Bowman, K.W.; Lee, M.; Henze, D.K.; Bousserez, N.; Brix, H.;
Collatz, G.J.; Menemenlis, D.; Ott, L.; Pawson, S.; Jones, D.; Nassar, R.:
**Carbon monitoring system flux estimation and attribution:
impact of ACOS-GOSAT XCO₂ sampling on the inference of
terrestrial biospheric sources and sinks**
In: Tellus B (2014) Blackwell Munksgaard

DOI: 10.3402/tellusb.v66.22486

1
2
3
4
5
6
7
8
9
10
11
12
13
14
15
16
17
18
19
20

Carbon Monitoring System Flux estimation and attribution (CMS-Flux): Impact of
ACOS-GOSAT X_{CO2} sampling on the inference of terrestrial biospheric sources and
sinks

*¹Junjie Liu, ¹Kevin Bowman, ¹Meemong Lee, ²Daven K. Henze, ²Nicolas Bousserez,
³Holger Brix, ⁴G. James Collatz, ¹Dimitris Menemenlis, ⁴Lesley Ott, ⁴Steven Pawson,
⁵Dylan Jones, ⁶Ray Nassar

¹Jet Propulsion Laboratory, California Institute of Technology; ² University of Colorado,
Boulder; ³University of California, Los Angeles, now at: Institute of
Coastal Research, Helmholtz-Zentrum Geesthacht, Germany; ⁴ NASA Goddard Space
Flight Center; ⁵University of Toronto; ⁶Environment Canada

Copyright 2014. All rights reserved.

March 13th, 2014

*Corresponding author Email: junjie.liu@jpl.nasa.gov

Abstract

1
2 Using an Observing System Simulation Experiment (OSSE), we investigate the impact of
3 JAXA Greenhouse gases Observing SATellite “IBUKI” (GOSAT) sampling on the
4 estimation of terrestrial biospheric flux with the NASA Carbon Monitoring System Flux
5 (CMS-Flux) estimation and attribution strategy. The simulated observations in the OSSE
6 use the actual column carbon dioxide (X_{CO_2}) b2.9 retrieval sensitivity and quality control
7 for the year 2010 processed through the Atmospheric CO₂ Observations from Space
8 algorithm. CMS-Flux is a variational inversion system that uses the GEOS-Chem forward
9 and adjoint model forced by a suite of observationally constrained fluxes from ocean,
10 land, and anthropogenic models. We investigate the impact of GOSAT sampling on flux
11 estimation in two aspects: 1) random error uncertainty reduction, and 2) the global and
12 regional bias in posterior flux resulted from the spatiotemporally biased GOSAT
13 sampling. Based upon Monte Carlo calculations, we find that global average reduction in
14 the flux uncertainty ranges from 25% in September to 60% in July. When aggregated to
15 the 11 land regions designated by the phase 3 of the Atmospheric Tracer Transport Model
16 Intercomparison Project, the annual mean uncertainty reduction ranges from 10% over
17 North American boreal to 38% over South American temperate, which is driven by
18 observational coverage and the magnitude of prior flux uncertainty. The uncertainty
19 reduction over the South American tropical region is 30%, even with sparse observation
20 coverage. We show that this reduction results from the large prior flux uncertainty and
21 the impact of non-local observations. Given the assumed prior error statistics, the degree
22 of freedom for signal is ~ 1132 for one-year of the 74,055 GOSAT X_{CO_2} observations,
23 which indicates that GOSAT provides ~ 1132 independent pieces of information about

1 surface fluxes. We quantify the impact of GOSAT's spatiotemporally sampling on the
2 posterior flux, and find that a 0.7 gigatons of carbon bias in the global annual posterior
3 flux resulted from the seasonally and diurnally biased sampling when using a diagonal
4 prior flux error covariance.

1 **1. Introduction**

2 Because of the crucial role of carbon dioxide (CO₂) in forcing climate (e.g., Mann et al.,
3 1998) and the uncertainties related to carbon-climate feedbacks in global models (e.g.,
4 Cox et al., 2000; Friedlingstein et al., 2006), it is essential to monitor how CO₂ is changing
5 and what processes are causing these changes. While fossil-fuel consumption is the
6 dominant man-made source of CO₂ to the atmosphere, about 55% of those CO₂ emissions
7 to date have been absorbed by the ocean and land (e.g., Gloor et al., 2010). NASA
8 initiated the Carbon Monitoring System (CMS) (<http://carbon.nasa.gov/>,
9 <http://cmsflux.jpl.nasa.gov/>) integrated Emission/Uptake Flux Pilot project in 2010 to
10 explore the capability of global modeling, assimilation, and observations to attribute
11 changes in atmospheric CO₂ to spatially resolved fluxes. The purpose of this paper is to
12 describe the formulation and integrity of the atmospheric inversion system used in the
13 NASA CMS Flux estimation and attribution (CMS-Flux). In the CMS-Flux, the surface
14 CO₂ fluxes estimated from observation-constrained terrestrial and oceanic carbon models
15 are used to force an atmospheric transport model, after which atmospheric inversion
16 refines the fluxes to match atmospheric CO₂ observations. Following Chevallier et al.
17 (2005), an Observing System Simulation Experiment (OSSE) is applied to assess the
18 ability of the inverse flux estimation to reproduce a known spatiotemporal distribution of
19 surface fluxes, which can only be done through an OSSE. The simulated observations
20 have the same coverage and sensitivity as the Japan Aerospace Exploration Agency
21 (JAXA) Greenhouse gases Observing SATellite “IBUKI” (GOSAT, Yokota et al., 2009)
22 b2.9 retrievals (O’Dell et al., 2012, Crisp et al., 2012) produced by the NASA
23 Atmospheric CO₂ observations from Space (ACOS) algorithm, which will also be used

1 with the forthcoming NASA Orbital Carbon Observatory (OCO-2) satellite (Crisp et al,
2 2008).
3
4 Chevallier et al. (2009, 2010b) have examined the impact of simulated GOSAT
5 observations on the flux estimation under both perfect and imperfect model assumptions.
6 The GOSAT sampling used in these studies was based on simulated retrieval throughput,
7 i.e., samples removed under cloudy conditions. There is no OSSE study so far that uses
8 the real GOSAT retrieval sampling and sensitivities, and few studies (Corbin et al., 2008;
9 Parazoo et al., 2012) have discussed the impact of spatiotemporally biased sampling on
10 CO₂ flux estimation. Sampling the simulated observations with the same observation
11 coverage and sensitivity as the real GOSAT b2.9 retrievals, we aim to address the
12 following questions:

- 13 1) What is the most optimistic impact of GOSAT b2.9 observations on the accuracy
14 and precision of inferred fluxes with the CMS-Flux?
- 15 2) What are the implications of GOSAT spatiotemporally biased sampling on
16 estimates of global and regional fluxes, e.g., in the northern high-latitudes?

17 Following Chevallier et al, (2007), we calculate posterior flux uncertainty from a Monte
18 Carlo method (Chevallier et al., 2007). In the CMS-Flux, we use variational data
19 assimilation to estimate monthly mean surface CO₂ flux at each model grid point. The
20 GEOS-Chem forward model (Nassar et al., 2010) is used to provide a link between
21 surface CO₂ fluxes and their impact on atmospheric CO₂ concentrations at later times.
22 The GEOS-Chem adjoint model (Henze et al., 2007) is used to calculate the sensitivity of

1 CO₂ concentration to the surface CO₂ flux at each grid point, which makes it possible to
2 estimate surface CO₂ flux at high spatiotemporal resolution.

3

4 The paper is structured as follows: Section 2 describes the CMS-Flux attribution strategy
5 including the GEOS-Chem forward and adjoint models, surface fluxes, variational
6 inversion method, simulated observations, inversion setup, and uncertainty
7 quantification; we discuss the results in Section 3 and summarize the major conclusions
8 in Section 4.

9 **2. CMS-Flux attribution strategy**

10 ***2.1 GEOS-Chem CO₂ forward and adjoint models***

11 GEOS-Chem is a global chemical transport model (CTM) driven by meteorological fields
12 from NASA's Goddard Earth Observing System, Version 5 (GEOS-5) data assimilation
13 system (Rienecker et al., 2008). Suntharalingam et al. (2004) describes an early
14 implementation of CO₂ simulation into GEOS-Chem, in which CO₂ is simulated as a
15 passive tracer forced by emissions from biomass burning, biofuel burning, fossil fuel
16 emissions, and cement manufacture, as well as by CO₂ exchange between the atmosphere
17 and the ocean and the terrestrial biosphere. Nassar et al. (2010) made a number of
18 updates including the addition of CO₂ forcing from shipping, aviation (3-D), and a
19 chemical source (3-D) into GEOS-Chem v8-03-02. They found that this simulation better
20 represented the observed latitudinal gradients than the previous version when compared
21 to surface-based and aircraft observations. The same version of GEOS-Chem has been
22 used to estimate surface fluxes using a synthesis Bayesian inversion constrained by mid-
23 tropospheric CO₂ from the Tropospheric Emission Spectrometer (Nassar et al., 2011).

1 The present study uses the same categories of CO₂ flux as Nassar et al. (2010, 2011), but
2 the fluxes are updated to represent our best prior knowledge for the year 2010.

3
4 The GEOS-Chem CO₂ adjoint model is based on the full-chemistry GEOS-Chem adjoint
5 model (Henze et al., 2007), which has been applied to estimate inorganic fine particles
6 (PM_{2.5}) precursor emissions over the United States (Henze et al., 2009), estimate carbon
7 monoxide (CO) emissions (Kopacz et al., 2009, 2010), and attribute direct ozone
8 radiative forcing (Bowman and Henze, 2012). The GEOS-Chem CO₂ adjoint model has
9 been thoroughly tested (Appendix A) following the methodology described in Henze et
10 al. (2007). It is publicly available ([http://wiki.seas.harvard.edu/geos-](http://wiki.seas.harvard.edu/geos-chem/index.php/GEOS-Chem_Adjoint)
11 [chem/index.php/GEOS-Chem_Adjoint](http://wiki.seas.harvard.edu/geos-chem/index.php/GEOS-Chem_Adjoint)). The version we use is v32.

12
13 The horizontal grid dimensions for both the forward and adjoint models are 4° (latitude)
14 × 5° (longitude), which allows a reasonable balance between a long assimilation window
15 and practical computational cost. There are 47 vertical levels with the top at about 0.01
16 hPa. This spatial resolution is sufficient to capture the large-scale atmospheric transport,
17 which is the primary driver of column CO₂ (X_{CO₂}) variability (Keppel-Aleks et al., 2011).

18

19 ***2.2 Surface CO₂ fluxes for 2010***

20 The surface CO₂ fluxes include emissions from fossil fuel, shipping, aviation, biofuel,
21 and biomass burning. The model also includes air-sea fluxes, terrestrial biosphere fluxes,
22 and secondary chemical sources within the atmosphere. The detailed carbon budgets and
23 sources for each category of the fluxes are listed in Table 1. Monthly fossil fuel emissions

1 are taken from the Carbon Dioxide Information Analysis Center (CDIAC, Andres et al.,
2 2011). The biomass burning emissions are from the daily Global Fire Emission Database
3 (GFED) v3 (van der Werf et al., 2010; Mu et al., 2010).

4
5 Three-hour air-sea fluxes are obtained from an observationally-constrained simulation
6 carried out using the ECCO2-Darwin configuration of the Massachusetts Institute of
7 Technology general circulation model (MITgcm, Marshall et al., 1997a,b). The
8 Estimating the Circulation and Climate of the Ocean, Phase II (ECCO2) project provides
9 a data-constrained estimate of the time-evolving physical ocean state (Menemenlis et al.,
10 2005, 2008), and the Darwin project provides time-evolving ecosystem variables
11 (Follows et al., 2007; Follows and Dutkiewicz, 2011; Dutkiewicz et al., 2009). Together,
12 ECCO2 and Darwin provide a time-evolving physical and biological environment for
13 carbon biogeochemistry, which is used to compute surface carbon fluxes at high spatial
14 resolution (18-km horizontal grid spacing). For this work, the fluxes are bin-averaged to a
15 $4^\circ \times 5^\circ$ grid. Compared to monthly mean fluxes from the Takahashi et al. (2002) atlas,
16 the three-hour air-sea fluxes from ECCO2-Darwin shows stronger variability in both
17 space and time (not shown).

18
19 Two sets of terrestrial biosphere fluxes are used. Both fluxes are three-hourly. One is
20 used as a “true” flux that acts as the boundary forcing in the “*nature run*”. This
21 simulation will be sampled along with GOSAT orbit to create a suite of observations. The
22 other biospheric flux is used as the prior flux for the “control” inversion. This prior flux
23 is the sum between a run of the Carnegie-Ames-Stanford-Approach (CASA) balanced

1 biosphere model (Randerson et al., 1997) and the scaled annual mean net CO₂ flux from
2 Phase 3 of the Atmospheric Tracer Transport Model Intercomparison Project
3 (TransCom3; Gurney et al., 2003). It is intended to represent a “climatological” state for
4 the inversion. The “true” terrestrial biosphere flux was computed as part of the CMS-
5 Flux, using an updated version of CASA that also includes impacts of biomass burning
6 from GFED v3 (van der Werf et al., 2004, 2006, 2010). The CASA-GFED3 flux
7 estimates were computed at monthly time steps with 0.5° spatial resolution. CASA-
8 GFED3 is a light use efficiency type model in which net primary productivity (NPP) is
9 expressed as the product of photosynthetically active solar radiation, a light use
10 efficiency parameter, scalars that capture temperature and moisture limitations, and
11 fractional absorption of solar radiation by the vegetation canopy (FPAR). The
12 heterotrophic respiration, R_h , is coupled to NPP via nine detrital carbon pools in which
13 decomposition is controlled by meteorological conditions and pool-dependent turnover
14 rates. Input data sets include meteorological data (air temperature, precipitation, and
15 incident solar radiation), a soil classification map, and a number of satellite-derived
16 products that characterize vegetation state and burned area (van der Werf et al., 2010).
17 For this study, NASA’s Modern-Era Retrospective Analysis for Research and
18 Applications (MERRA) meteorology (Rienecker et al., 2011) was used and FPAR was
19 derived from the Advanced Very High Resolution Radiometer Normalized Difference
20 Vegetation Index (AVHRR NDVI) (Tucker et al., 2005) according to the procedure of
21 Los et al. (2000). The monthly CO₂ fluxes were disaggregated to three-hour values with
22 GEOS-5 temperature and radiation analysis fields following Olsen and Randerson (2004)
23 and aggregated to the 4° × 5° grid for the atmospheric model.

1

2 The true and the prior terrestrial biosphere fluxes have the same annual totals globally (-
3 5.3 GtC), but they have different seasonal and diurnal cycles and spatial patterns,
4 especially in the tropics. As shown in Figure 1, both the seasonal and diurnal cycles of
5 the prior flux over the Northern Hemisphere (NH) are weaker. To some extent, the
6 difference between the prior flux used in the control inversion and the true flux reflects
7 the current understanding of the carbon cycle: the global net flux (which is well
8 constrained by the atmospheric CO₂ observations) is less uncertain than the spatial and
9 temporal distribution of this net flux (Le Quere et al, 2013).

10

11 ***2.3 Simulated ACOS-GOSAT b2.9 observations***

12 We simulate the ACOS-GOSAT X_{CO2} observations with the same observation coverage
13 and vertical sensitivity as the ACOS-GOSAT b2.9 retrievals (O'Dell et al., 2012).

14 GOSAT is the first successfully launched satellite that is dedicated to observe CO₂ and

15 methane (CH₄) column abundances with the Thermal And Near Infrared Sensor for

16 Carbon Observation-Fourier Transform Spectrometer (TANSO-FTS; Yokota et al.,

17 2009). It started operation in February 2009, and it orbits the globe with a polar sun-

18 synchronous trajectory. The descending orbits cross the Equator at about 13:00 local

19 solar time. The orbits repeat every 90-100 minutes at that same local solar time. The

20 ground track repeats every three days. In the near infrared, GOSAT measures sunlight

21 reflected from the surface, and thus represents information about the entire atmospheric

22 column that includes sensitivity to boundary layer CO₂ concentrations. Over land,

23 TANSO-FTS points to nadir, with a 10.5-km diameter circular footprint. Over the ocean,

1 TANSO-FTS points to the glint spot in order to compensate for the low reflectivity of the
2 ocean in the nadir viewing direction.
3
4 The throughput of real GOSAT retrievals is less than the full satellite coverage as a
5 consequence of cloud contamination, poor retrieval quality, etc. In order to incorporate
6 these effects, the simulated ACOS-GOSAT b2.9 observations are filtered according to
7 the recommendations of the ACOS b2.9 Level 2 Standard Product Data User's Guide
8 (available at <http://oco.jpl.nasa.gov/ocodatacenter/>). Only the nadir-view high-gain
9 observations with master quality flag equal to one are simulated: the medium-gain land
10 observations and the ocean glint data are not used. The master quality flag provided in the
11 b2.9 retrieval product considers the confidence in the retrieved X_{CO_2} (see ACOS Level 2
12 Standard Product Data User's Guide, b2.9). Glint measurements are made exclusively
13 over ocean and have different properties than the nadir measurements made over land
14 (Wunch et al., 2011). The excluded medium-gain TANSO-FTS mode, which is used over
15 bright surface scenes (e.g., over the desert) is known to have ghosting issues caused by
16 mismatched timing delays in the signal chain (Wunch et al., 2011). The filtered
17 observation coverage is non-uniform in both space and time (Figure 2). A significant
18 portion of the tropical region is not observed due to cloud contamination (Figure 2b). The
19 unobserved region closely follows the movement of the Inter-Tropical Convergence Zone
20 (ITCZ). When the ITCZ moves to the northern part of the Equator during summer, so
21 does the unobserved region. There are less than 20 observations at most of the grid points
22 over north of the Amazon during 2010 (Figure 2a). Over the NH high latitudes (north of
23 40°N), the coverage is seasonally dependent; there are no observations during late fall,

1 winter, and early spring due to the reduced signal-to-noise ratio from the low solar zenith
2 angle. The total number of good-quality observations after filtering is 74,055 for 2010.
3 We simulate the observations at the ACOS-GOSAT b2.9 locations without any spatial
4 averaging. Since two observations close in space and time (i.e., observed in the same grid
5 box within an hour) may contain the same surface flux information, some of the
6 observations provide redundant information about surface fluxes. These redundant
7 observations improve precision through implicit averaging in the inversion system. The
8 amount of simulated ACOS-GOSAT observations assimilated in this study is much less
9 than the total 330,000 GOSAT observations simulated in Chevallier et al. (2010b), which
10 is partly because we do not simulate glint-mode GOSAT observations over ocean areas
11 and the stricter quality control of the real retrieving process.

12

13 We generate simulated observations based on CO₂ vertical profiles, \mathbf{c}^t , from the nature
14 run that is forced by the true terrestrial biosphere flux. The nature run output interval is
15 hourly. We first sample the simulated CO₂ profiles, \mathbf{c}^t , at the closest times and locations
16 of the real good-quality ACOS-GOSAT b2.9 observations. We then apply an observation
17 operator, $h(\cdot)$ (Equation 1), to calculate the model simulated X_{CO_2} . The model simulated
18 X_{CO_2} at the i^{th} location y_i^t can be written as:

$$19 \quad y_i^t = y_i^b + \mathbf{a}_i^T \cdot (\mathbf{c}_i^t - \mathbf{c}_i^b) \quad (1)$$

20 where \mathbf{a}_i is the GOSAT column averaging kernel, and \mathbf{c}_i^b and y_i^b are the a priori CO₂
21 profile and the a priori X_{CO_2} assumed in the GOSAT X_{CO_2} retrieval process. These three

1 quantities are from the ACOS-GOSAT b2.9 retrieval products. The simulated ACOS-
2 GOSAT X_{CO_2} retrieval vector \mathbf{y}^o is the model simulated X_{CO_2} \mathbf{y}^f with random errors:

$$3 \quad \mathbf{y}^o = \mathbf{y}^f + \mathbf{e}^o \quad (2)$$

4 where the elements of vector \mathbf{e}^o are the random observation errors. The i^{th} element of the
5 vector \mathbf{y}^f is equal to y_i^f . The random observation error \mathbf{e}^o can be rewritten as:

$$6 \quad \mathbf{e}^o = \mathbf{r} \cdot \mathbf{p} \quad (3)$$

7 where the elements of vector \mathbf{r} are the estimated observation errors of real ACOS-
8 GOSAT observations that comes along with the ACOS-GOSAT b2.9 retrieval products.

9 The vector \mathbf{p} consists of Gaussian distributed random numbers with zero mean and unity
10 standard deviation. The observation error covariance then can be written as

11 $\mathbf{R} = E[\mathbf{e}^o (\mathbf{e}^o)^T]$, where $E[\cdot]$ represents the expectation operator. We assume there is no
12 error correlation among observations, so the observation error covariance \mathbf{R} is a diagonal
13 matrix with values ranging between one ppm^2 and nine ppm^2 for most samples. The
14 amount of observation information could be less if there were error correlations among
15 observations, which can result from calibration errors or systematic errors in the
16 atmospheric state, e.g., surface pressure. We assume no transport errors, since we use the
17 same transport model in both the flux inversion and the observation generation. We also
18 ignore any systematic biases in GOSAT observations, whose impact on flux estimation
19 has been discussed before (e.g., Baker et al., 2010; Basu et al. 2013). Therefore, the
20 GOSAT observation impact obtained from this study is the most optimistic estimate.
21 Neglecting these errors also allows us to focus on the fundamental role of coverage and
22 sampling on the inference of surface CO_2 fluxes.

23 *2.4 Flux attribution with variational data assimilation*

1 The variational data assimilation solves for a control vector \mathbf{x} by iteratively minimizing
 2 the following cost function:

$$3 \quad J(\mathbf{x}) = \frac{1}{2}[(\mathbf{x} - \mathbf{x}_0)^T \mathbf{B}^{-1}(\mathbf{x} - \mathbf{x}_0)] + \frac{1}{2}[(\mathbf{y}^o - h(M(\mathbf{x} \cdot \mathbf{f}^b + \mathbf{f}^d)))^T \mathbf{R}^{-1}(\mathbf{y}^o - h(M(\mathbf{x} \cdot \mathbf{f}^b + \mathbf{f}^d)))]$$

4 (4)

5 where \mathbf{y}^o is the simulated ACOS-GOSAT X_{CO_2} defined in Equation (2). The control
 6 vector \mathbf{x} defines temporally varying and spatially gridded scale factors, which are
 7 applied to the prior monthly mean flux, \mathbf{f}^b . For this application, the scale factors are
 8 monthly at each $4^\circ \times 5^\circ$ grid point. The prior scale vector, \mathbf{x}_0 , is equal to one
 9 everywhere, and its error covariance matrix is \mathbf{B} (section 2.5). GEOS-Chem forward
 10 model $M(\cdot)$ simulates CO_2 vertical profiles from the surface flux $\mathbf{x} \cdot \mathbf{f}^b + \mathbf{f}^d$, where \mathbf{f}^d
 11 represents the 3-hourly diurnal fluxes that have zero monthly mean value at every grid
 12 point. The diurnal flux \mathbf{f}^d is not optimized. Based on Equation (1), the observation
 13 operator $h(\cdot)$ calculates the model simulated X_{CO_2} from CO_2 vertical profiles at the
 14 closest times and locations of ACOS-GOSAT b2.9 observations.

15
 16 The optimized scale factor is the scale factor that minimizes the cost function defined in
 17 Equation (4). To minimize the cost function, we use the Limited-memory Broyden–
 18 Fletcher–Goldfarb–Shanno (L-BFGS; Byrd et al., 1994; Zhu et al., 1997) numerical
 19 minimization scheme. It is the no-bound option of the L-BFGS-B (Bounded) algorithm,
 20 i.e., L-BFGS. The L-BFGS algorithm requires the gradient of the cost function

$$21 \quad \frac{\partial J}{\partial \mathbf{x}} = \mathbf{M}^T \mathbf{H}^T \mathbf{R}^{-1}[\mathbf{y}^o - h(M(\mathbf{x} \cdot \mathbf{f}^b + \mathbf{f}^d))] + \mathbf{B}^{-1}(\mathbf{x} - \mathbf{x}_0) \quad (5)$$

1 where \mathbf{H} is the linearized observation operator $h(\cdot)$, and \mathbf{H}^T is its adjoint. The operator
2 \mathbf{M}^T is the adjoint of the GEOS-Chem model. The L-BFGS algorithm iteratively adjusts
3 the control vector until the cost function reaches a minimum. We assess the convergence
4 by defining a stopping criterion when the ratio between the cost function and the number
5 of the observations is close to one. This standard is chosen in consideration of both
6 inversion convergence (section 3.1) and computational cost of the minimization. In our
7 case, a single iteration using one year of data takes about 5.5 central processing unit
8 (CPU) hours when using two quad-core processors operating at 3 GHz.

9 *2.5 Inversion setup*

10 In this OSSE study, we solely optimize the terrestrial biosphere flux, assuming perfect
11 flux from the other sources and perfect initial state of CO₂. However, we consider the
12 error propagation from non-terrestrial biosphere flux into the terrestrial biosphere flux
13 when constructing the biosphere flux prior error statistics, which will be discussed later in
14 this section. We choose not to optimize ocean flux, because of the sparse coverage of
15 ACOS-GOSAT b2.9 observations over ocean (not shown). The assimilation window is
16 one year. The control vector is twelve monthly scale factors defined at each grid point.
17 We note that the system can also estimate all types of fluxes (e.g., fossil fuel, ocean, and
18 land) at the native GEOS-Chem spatial resolution and at finer time scales.

19

20 The prior flux error covariance matrix, \mathbf{B} , is one of the key elements needed for an
21 optimal flux estimate, and it is quite challenging to characterize (Michalak et al., 2005;
22 Chevallier et al., 2012). In this study, the prior flux error statistics were constructed from
23 a Monte Carlo run of CASA-GFED 3 by sampling the distributions of model parameters.

1 The square root of the sum of the error variances over the globe for the individual fluxes
2 has been scaled to be equal to 1.0 GtC/year, which is the 2010 terrestrial biosphere flux
3 uncertainty published by Global Carbon Project (<http://www.globalcarbonproject.org/>).
4 This uncertainty considers the uncertainty propagation from non-biosphere fluxes (fossil
5 fuel, land use, and ocean) to biosphere fluxes. Since we estimate monthly mean flux scale
6 factors, we scale the terrestrial biosphere flux error statistics by the absolute value of the
7 prior monthly mean flux. We set the lower bound of the scaled errors to be 0.05 and the
8 upper bound to be 1.0. The lower bound is to ensure that the observations can always
9 have some impact on the surface flux estimation, since the impact of the observations is
10 weighted against the prior error statistics (Equation (4)). The upper bound is to avoid
11 spuriously high values in the prior flux error statistics for the near-zero prior flux. The
12 scaled errors change monthly at each grid point, and they are used as the square root of
13 diagonal elements in a prior error covariance matrix **B**. Due to the spatial inhomogeneity
14 of the terrestrial biosphere flux and the coarse resolution of our inversion, we assume
15 there is no spatial error correlation between different grid points. We also assume no
16 error correlation between different months, even though the difference between the true
17 flux and the prior flux indicates a seasonal anti-correlation, especially over the NH.
18 Neglecting this temporal correlation will degrade the final posterior flux estimate, which
19 we will be further discussed in section 3.2.2. Therefore, the prior flux error covariance
20 matrix **B** is diagonal. In Figure 3, we plot the equivalent prior error statistics in flux. The
21 magnitude of the prior flux error statistics is larger over the tropics, Eurasia, and eastern
22 North America (Figure 3a). The tropical uncertainty is relatively high with respect to the
23 NH uncertainty even though the NH flux is higher in absolute terms. The errors are larger

1 during boreal summer in the NH and the whole year in the southern part of the tropical
2 region (Figure 3b).

3

4 *2.6 Posterior flux uncertainty quantification with a Monte Carlo approach*

5 Theoretically, the posterior flux error covariance can be calculated from a number of
6 analytical equations (e.g., Kalnay, 2003; Tarantola, 2005). However, the large dimension
7 of the state vector \mathbf{x} prohibits a direct calculation of this covariance. In this study, the
8 posterior flux uncertainty is approximated using a Monte Carlo approach (Chevallier et
9 al., 2007). In the Monte Carlo approach, an ensemble of prior states and observations are
10 generated, consistent with the prior and observation error statistics. Then the standard
11 deviation of the ensemble posterior fluxes gives the posterior flux uncertainty. The mean
12 of the ensemble prior states is equal to the true flux. Different from the control inversion,
13 the ensemble prior fluxes have the same diurnal cycle and seasonal cycle as the true flux.
14 We performed 60 flux estimates. We chose 60 ensembles in consideration of both the
15 computational cost and the reasonableness of the uncertainty reduction in aggregated
16 large spatial and temporal scale.

17

18 The 60 sets of simulated observations are the “true” ACOS-GOSAT with 60 different
19 sets of random errors generated according to Equation (3). The ensemble prior fluxes are
20 the true flux \mathbf{f}^t perturbed by random errors, which have the same statistics as the
21 specified scaled prior flux error covariance \mathbf{B} . The prior flux of the n^{th} ensemble member
22 \mathbf{f}_n^b is generated according to the following:

$$23 \quad \mathbf{f}_n^b = \mathbf{f}^t + \mathbf{B}^{\frac{1}{2}} \cdot \mathbf{Q}_n \cdot \mathbf{f}^t \quad (6)$$

1 where \mathbf{Q}_n is a diagonal matrix whose elements are Gaussian distributed random numbers
2 with zero mean and unity standard deviation.
3
4 We define the uncertainty reduction at each point as $1 - \sigma_a / \sigma_b$, where σ_a and σ_b are the
5 standard deviations of the ensemble posterior and prior fluxes respectively at a specific
6 time and location. The uncertainty reduction $1 - \sigma_a / \sigma_b$ indicates the random error
7 uncertainty reduction. In the later discussion, we define “*error*” as the absolute difference
8 between the posterior flux from the control inversion and the true flux, and the
9 “*uncertainty*” as the standard deviation of ensemble prior/posterior fluxes in the Monte
10 Carlo flux estimation.

11 **3. Results**

12 In this section, we first evaluate convergence and degrees of freedom for signal (DFS).
13 Then, we discuss the impact of assimilating simulated ACOS-GOSAT observations on
14 CO₂ flux estimation in two aspects: 1) random error uncertainty reduction; and 2) the
15 consequence of ACOS-GOSAT spatiotemporally biased sampling on the estimated
16 annual flux at both the global and regional scales. Finally, through forward perturbation
17 simulation experiments, we analyze the impact of remote CO₂ observations on flux
18 estimation over the South American Tropical region, where the observation coverage is
19 sparse.

20 **3.1 Convergence and Degrees of Freedom for Signal**

21 In an optimal system, the minimum of the cost function is chi-square distributed with
22 expectation and variance equal to the number of observations. We stopped iterating after
23 70 iterations in the control inversion, when the ratio between the cost function and the

1 total number of observations reaches 1.17. This indicates that the solution is close to
2 convergence. The reason that it has not reached 1.0 yet is because the difference between
3 the prior and the true flux is not totally random (Figure 1) and the suboptimal prior flux
4 error covariance. With Monte Carlo ensemble runs, where the difference between the
5 prior and the true flux is completely random, the ratio between the cost function and the
6 number of observations reaches 1.0 after about 20 iterations (not shown).

7

8 Given the prior information, the number of independent pieces of information that the
9 assimilated observations provide can be described by the DFS (e.g., Rodgers, 2000). It is
10 defined as

$$11 \quad d_s = E[(\mathbf{x}_a - \mathbf{x}_0)^T \mathbf{B}^{-1}(\mathbf{x}_a - \mathbf{x}_0)] \quad (7)$$

12 where \mathbf{x}_a is the optimized vector. DFS based on the ensemble inversions performed in
13 the uncertainty quantification is ~ 1132 . This indicates that the 74055 GOSAT X_{CO_2}
14 observations provide ~ 1132 independent observables about the fluxes given the assumed
15 prior flux error statistics. This number is much smaller than the size of our *control* vector,
16 which is 11,923 (one-third of total grid points), or 993 spatial-resolved fluxes per month.
17 Consequently, the GOSAT X_{CO_2} can constrain about 10% of the spatiotemporal fluxes
18 over the year. If we assume that the DFS is distributed evenly as a function of month,
19 then the current system could resolve roughly 100 locations. The actual number will be
20 higher in the NH summer and smaller in the NH winter. The DFS is still substantially
21 higher than the number of TransCom 3 regions.

22 **3.2 Posterior flux**

23 **3.2.1 Global flux seasonal cycle**

1 Figure 4 shows posterior flux seasonal cycle averaged over the globe (red line in Figure
2 4a), and its flux uncertainty reduction as a function of month (Figure 4b). The global
3 averaged flux seasonal cycle has been improved (Figure 4a), especially during the later
4 half of the year when the prior flux (blue line) and the true flux (black line) differ the
5 most. The monthly mean flux uncertainty reduction (Figure 4b) is in the range of 25–60%
6 with the reduction being largest during the boreal summer when the observation coverage
7 is most dense. The small uncertainty reduction in December is due to two factors: sparse
8 observation coverage over the NH high latitudes during winter and proximity to the
9 assimilation window terminus. There are fewer observations to constrain December
10 fluxes as opposed to, say, January fluxes where observations over the entire assimilation
11 window can in principle provide a constraint. We can overcome the second factor by
12 extending the assimilation window to more than one year, e.g., 15 months, but only
13 analyzing the flux of the first 12 months.

14 **3.2.2 Global annual flux and its relationship with observation sampling**

15 In this sub-section, we discuss the consequence of ACOS-GOSAT spatiotemporally
16 biased sampling on the estimated annual flux at the global scale under the condition of
17 our specific inversion setup. Averaged zonally, the seasonality of the posterior flux from
18 the control inversion has been improved over all latitudes (Figure 1f). The RMS error of
19 the monthly zonal mean flux has been reduced by as much as 50% (Figure 1g).
20 However, the annual global total flux has become -6.0 GtC/year after optimization. It is
21 worse than the prior flux (-5.3 GtC/year), which is constructed to be equal to the true
22 annual flux. Spatially, the annual mean flux also becomes worse over some locations, for
23 example, over Europe (Figure 1c). Why does the annual flux become worse while the

1 monthly zonal mean flux is improved in all months? We find that the extra 0.7 GtC/year
2 sink in the annual total posterior flux is due to both the specific inversion setup and the
3 difference between the observed value forced by the true flux and the model-predicted
4 observations forced by the prior flux. Since the prior flux error covariance matrix is
5 diagonal (section 2.6), the adjustment to the prior flux during inversion would be more
6 subject to the difference between the observations and the model simulated values than
7 otherwise. Averaged over the globe, the annual mean simulated ACOS-GOSAT X_{CO_2}
8 forced by the true flux is 387.12 ppm, and the annual mean simulated ACOS-GOSAT
9 X_{CO_2} forced by the prior flux is 387.49 ppm. If we assume that an equivalent net CO_2 flux
10 into the atmosphere is the same between a 1-ppm increase in ACOS-GOSAT X_{CO_2} and a
11 1-ppm increase in the global mean CO_2 provided NOAA (<http://www.esrl.noaa.gov/>), the
12 0.37-ppm difference is equivalent to 0.8 GtC/year since a 1-ppm increase in global mean
13 CO_2 is equivalent to a ~ 2.1276 GtC net CO_2 flux into the atmosphere (Gruber et al., 2009;
14 Sarmiento et al., 2010). The 0.1 GtC difference from the actual posterior flux bias is
15 because the CO_2 has not been well mixed towards the end of the year, which affects the
16 accuracy in transferring CO_2 difference into flux. As we shall show, this 0.37-ppm
17 difference is a consequence of the sampling of GOSAT.

18

19 In order to better understand where the 0.37-ppm difference comes from, we plot 10-day
20 running-mean X_{CO_2} from the nature run sampled with different strategies in Figure 5a.
21 X_{CO_2} here is a pressure-weighted column CO_2 without using the ACOS-GOSAT
22 averaging kernels. When only sampled at the ACOS-GOSAT locations and times (black
23 line), the annual mean X_{CO_2} is 0.14 ppm smaller than the annual mean X_{CO_2} sampled at

1 all grid points every three hours (blue line). This difference is a combination effect of
2 ACOS-GOSAT seasonally dependent partial geographic sampling and daytime only
3 sampling. When we sample X_{CO_2} at ACOS-GOSAT locations every three hours (red line
4 in Figure 5a and b), the annual mean X_{CO_2} is 0.05 ppm smaller than the annual mean
5 X_{CO_2} sampled at all grid points every three hours. When only sampled at the ACOS-
6 GOSAT observing time, the annual mean X_{CO_2} is 0.09 ppm smaller than the annual mean
7 X_{CO_2} sampled every three hours, even though both strategies sample the same ACOS-
8 GOSAT locations. It indicates that the ACOS-GOSAT daytime only sampling results in -
9 0.09-ppm bias, while partial geographic sampling introduces -0.05-ppm bias. The low
10 bias from the daytime only sampling is because the terrestrial biosphere absorbs CO_2
11 from the atmosphere during the daytime. Miller et al. (2007) show that the X_{CO_2} sampled
12 at 13:00 pm (local time) is most close to daily average X_{CO_2} . However, the difference
13 between X_{CO_2} sampled at 13:00 pm and the daily average X_{CO_2} depends on the magnitude
14 and phase of terrestrial biosphere diurnal cycle. The seasonally dependent sampling
15 introduces a low bias in X_{CO_2} is because of the ACOS-GOSAT preferentially samples in
16 the NH high latitudes during summer, which is the time of significant carbon uptake from
17 terrestrial biosphere, while having a relatively low spatial sampling yield in the late fall
18 and winter.

19

20 The above analysis about the nature run X_{CO_2} sampled with different strategies implies
21 that two X_{CO_2} fields sampled at ACOS-GOSAT locations and times could have different
22 annual mean values when the surface CO_2 fluxes have different diurnal and seasonal
23 cycles, even with the same annual flux, as is the case here. Compared to the prior flux

1 used in the control inversion, the true flux has a stronger seasonal cycle (Figure 1) and
2 diurnal cycle (not shown), especially over the NH. ACOS-GOSAT tends to sample the
3 locations and times when the biosphere absorbs CO₂ from the atmosphere, e.g., daytime
4 and boreal summer, so the observations have a lower value than the X_{CO2} forced by the
5 prior flux when sampled at ACOS-GOSAT locations and times (black line in Figure 5c).
6 In order to disentangle the contribution of diurnal biased sampling from the seasonally
7 dependent sampling, we run a CO₂ simulation, in which the terrestrial biosphere flux has
8 the same diurnal cycle as the true flux while maintaining the same seasonal cycle as the
9 prior flux used in the control run. The annual net flux from this combined flux is still -5.3
10 GtC/year. The annual mean difference between the observations and the X_{CO2} sampled at
11 the GOSAT locations and time (red line in Figure 5c) is -0.25 ppm, which is the
12 combination effect of the seasonally dependent sampling and the different seasonal cycle
13 between the true flux and the prior flux. It also implies that the diurnally biased sampling
14 in combination of the different diurnal cycle between the true flux and the prior flux
15 results in -0.12 ppm difference. Therefore, the 0.37-ppm difference between the
16 simulated ACOS-GOSAT X_{CO2} from the nature run and the simulated ACOS-GOSAT
17 X_{CO2} forced by the prior flux is due to the spatiotemporally dependent sampling of
18 ACOS-GOSAT X_{CO2} observations (Figure 3) in combination with the systematic
19 spatiotemporal difference between the true flux and the prior flux (Figure 1).

20

21 In order to further test whether the bias in the annual total posterior flux is due to ACOS-
22 GOSAT sampling, we did another experiment that assimilates the simulated X_{CO2}
23 observations with a random distribution in space and time, but with the same observation

1 error statistics and sensitivity as ACOS-GOSAT X_{CO_2} . We find that the posterior flux
2 (green line in Figure 4a) from this experiment is -5.4 GtC, much closer to the true flux (-
3 5.3 GtC) than the posterior flux with the GOSAT sampling characteristics. Compared to
4 the posterior flux constrained by ACOS-GOSAT X_{CO_2} (red line in Figure 4a), the
5 posterior flux assimilating the random sampled X_{CO_2} is much more accurate during the
6 winter months, when ACOS-GOSAT X_{CO_2} almost has no sampling over the high
7 latitudes. This experiment proves that the bias in the posterior flux when assimilating the
8 simulated ACOS-GOSAT X_{CO_2} is due to its spatiotemporally dependent sampling. Even
9 with ACOS-GOSAT, including a more realistic temporal error correlation (e.g., the
10 seasonal anti-correlation) would reduce the impact of the biased ACOS-GOSAT X_{CO_2}
11 sampling and therefore the bias in the annual total flux. However, as far as we know, the
12 current state-of-the-art inversion systems (e.g., Chevallier et al., 2007; Baker et al., 2010;
13 Basu et al., 2013) do not have such seasonal anti-correlation error statistics, which is due
14 to the computational cost and complexities of a large-scale inversion system. Without an
15 accurate seasonal cycle in the prior flux or the accurate prior flux error covariance, it
16 requires caution to interpret the annual total flux when assimilating GOSAT X_{CO_2} or
17 GOSAT-type X_{CO_2} observations.

18 ***3.2.3 Accuracy, uncertainty reduction, and biases of the posterior flux at TransCom 3*** 19 ***regions***

20 In this subsection, we discuss the impact of simulated ACOS-GOSAT observations on
21 the aggregated flux estimation at the 11 land regions (Figure 6 l) defined in TransCom 3.

22

1 The seasonal cycle over these 11 regions has been improved (Figure 6 a–k). The root
2 mean square (RMS) error reduction is between 35% and 63%, with the reduction being
3 around 50% over most of the regions. The posterior flux (red line) and the true flux
4 (black line) have the same seasonal cycle phase, even with a dissimilar phase in the prior
5 flux (blue line), e.g., in the tropics (Figure 6 d, f). The amplitude of the seasonal cycle has
6 also been improved. The magnitude of error reduction has a close relationship with the
7 number of observations assimilated (purple line in Figure 6 a-k). Over the NH boreal
8 region (Figure 6 a, g, k), during the winter when the observations are sparse, the posterior
9 flux error only becomes slightly smaller than the prior flux error; while during the boreal
10 summer when the observations are dense, the posterior flux has much smaller error than
11 the prior flux. Even though the monthly flux in all these TransCom 3 regions has been
12 improved, the annual mean flux becomes worse over some regions. For example, over
13 Europe, the RMS error of the monthly prior flux is $0.22 \text{ gC/m}^2/\text{day}$, and the RMS error of
14 the monthly posterior flux has been reduced to $0.12 \text{ gC/m}^2/\text{day}$. However, the annual
15 mean flux is $-0.22 \text{ gC/m}^2/\text{day}$ after optimization, while the true annual mean flux and the
16 prior flux are $-0.15 \text{ gC/m}^2/\text{day}$ and $-0.19 \text{ gC/m}^2/\text{day}$, respectively. This degradation of the
17 annual mean flux is due to the seasonally and diurnally biased sampling in combination
18 with the different seasonal cycle and diurnal cycle between the prior and the true flux as
19 discussed in section 3.2.2. ACOS-GOSAT observations capture the stronger sink during
20 summer, but they miss the stronger source during spring and winter in the true flux,
21 which results in the stronger annual posterior sinks over Europe and the North American
22 boreal region (Figure 1c, Figure 6 a, k). Including a seasonal anti-correlation in the prior
23 flux covariance would increase the source magnitude of the prior flux during winter and

1 spring when ACOS-GOSAT observations are not available, and therefore reduce the bias
2 in the annual total flux over Europe and The North American boreal region.

3

4 The uncertainty reduction of the monthly mean flux over the TransCom 3 regions ranges
5 from 10% over North American boreal to 38% over South American temperate
6 (Figure 7b). The magnitude of uncertainty reduction is related to both the prior flux error
7 (Figure 7a) and the observation coverage. Over North American boreal, both the total
8 number of observations (purple line in Figure 6f) and the prior flux error (Figure 7a) are
9 small, so the uncertainty reduction is small. Over the South American tropical region,
10 even though the total number of observations is small, only 1073, the uncertainty
11 reduction is still 30%, which is mainly due to the relatively large magnitude of the prior
12 flux uncertainty (Figure 7a) and the impact of remote observations (section 3.4).
13 Chevallier et al. (2009) showed that the fractional uncertainty reduction ranges from 25%
14 to 80% over terrestrial TransCom 3 regions when assimilating simulated GOSAT
15 observations without transport errors, which is larger than we find here. We speculate
16 that the main reason is due to the difference in the number of observations assimilated
17 (section 2.4).

18 ***3.3 The sensitivity of remote CO₂ concentrations to the surface flux over the South***

19 ***American Tropical region***

20 The South American Tropical region is home to one of the world's largest tropical
21 rainforests, and is experiencing rapid land-cover change (e.g., Lepers et al., 2005).
22 Understanding the carbon budget over this region is crucial to improve our understanding
23 of the global carbon cycle and the impact of human activity on ecosystems. However, due

1 to the lack of observation coverage so far, the carbon budget over this region still has a
2 large uncertainty (e.g., Stephens et al., 2007). We showed theoretically that ACOS-
3 GOSAT could reduce the flux uncertainty by 30% even with sparse observation coverage
4 over this region. In this subsection, through forward perturbation simulation experiment,
5 we examine contributions to the improvement aside from the local observations.

6

7 In this experiment, we perturb the prior flux in the control run over the South American
8 tropical region (rectangle in Figure 8) to equal the true flux in the nature run. We then
9 compare X_{CO_2} from this perturbation experiment to the X_{CO_2} from the original control
10 run. The perturbed region is a close approximation to the TransCom3 South American
11 tropical region. We find that the surface CO_2 flux over the perturbed region has an impact
12 on X_{CO_2} over South American temperate and South Africa (Figure 8a and b). These
13 regions have much denser observational coverage than over the perturbed region (Figure
14 8c and d). The monthly mean X_{CO_2} difference between the perturbed run and the control
15 run is about 0.2 ppm over South Africa, and the magnitude can be up to 0.8 ppm over
16 South American temperate. The instantaneous X_{CO_2} difference between the perturbed run
17 and the control run can be more than one ppm over these regions, which is significant
18 relative to the observation error statistics (one ppm to three ppm). When the Intertropical
19 Convergence Zone moves to the north of the Equator during boreal summer, the surface
20 CO_2 flux over the perturbed region also has large impact on the X_{CO_2} over Central to
21 North America (Figure 8a). This experiment indicates that the X_{CO_2} observations over
22 Central to North America during boreal summer and the X_{CO_2} observations over South
23 African and South American temperature regions have strong sensitivities to the CO_2 flux

1 over South American tropical region. Therefore, the posterior flux improvement over the
2 perturbed region is mainly from the impact of the observations over these regions, since
3 where the observation coverage is much denser than the observation coverage over the
4 perturbed region (Figure 1, Figure 8c and d). In this study, we do not consider transport
5 errors. Chevallier et al. (2010b) found that the largest bias happens in the South American
6 Tropical region when assimilating simulated GOSAT observations in the presence of
7 transport errors. When the model is imperfect, this remote connection between flux and
8 the X_{CO_2} may also lead to dipole surface CO_2 flux estimation (Stephens et al., 2007).
9 Figure 8a and b also show that the X_{CO_2} observations over the Eastern Tropical Pacific
10 and the South Atlantic Ocean have strong sensitivities to the flux over the perturbed
11 region. We expect that the assimilation of X_{CO_2} observations especially glint observations
12 over these oceanic regions could have a significant impact on the estimate of South
13 American tropical terrestrial biosphere flux.

14 **4 Discussion and Conclusions**

15 In this paper, we describe the variational inversion system developed as part of the CMS
16 Flux estimation and attribution (CMS-Flux) (<http://www.carbon.nasa.gov>,
17 <http://cmsflux.jpl.nasa.gov>), and demonstrate the performance of this system in the
18 context of an Observing System Simulation Experiment (OSSE). Using the same
19 coverage and sensitivity as the real ACOS-GOSAT b2.9 observations for 2010, we
20 further discuss the impact of GOSAT spatiotemporally biased sampling on the net flux
21 estimation, and the impact of remote observations on tropical flux estimation, where the
22 GOSAT has sparse observation coverage. The results from this OSSE help us understand

1 the impact of the unique ACOS-GOSAT spatiotemporal sampling on flux estimation. A
2 follow-on paper will describe the assimilation of real ACOS-GOSAT observations.

3

4 With Monte Carlo method, we quantified the random error uncertainty reduction in the
5 posterior flux. We carried out 60-member ensemble inversions, in which the ensemble
6 prior fluxes and the ensemble-simulated observations follow the error statistics used in
7 the inversion. The degree of freedom for signal is ~ 1132 , which indicates that a one-year
8 of total 74,055 GOSAT X_{CO_2} observations has ~ 1132 independent quantities about the
9 fluxes given the assumed prior flux error statistics. The results show that the uncertainty
10 reduction of the monthly global mean flux ranges from 25% to 60%. When aggregated to
11 TranCom3 regions, the monthly mean flux uncertainty reduction ranges from 10% over
12 North American boreal to 38% over South American temperate, where the observation
13 coverage is dense and the prior flux uncertainty has relatively large magnitude.

14

15 We also found that the ACOS-GOSAT observations can reduce the uncertainty over the
16 South American tropical region by 30% in spite of the sparse local observation coverage.
17 Through a sensitivity experiment, we illustrated that this large uncertainty reduction is
18 mainly from the observations over Central America, South American temperate, and
19 South Africa, where the CO_2 concentrations are sensitive to South American tropical
20 flux. Parazoo et al. (2013) show that the X_{CO_2} observations and Solar-induced
21 Chlorophyll Fluorescence (SIF) from GOSAT provide complementary information about
22 the net flux and the Gross Primary Production (GPP) over the Southern Amazonia region,

1 which indicates that we can use these two types of observations to disentangle respiration
2 and GPP over the broad Amazonia region.
3
4 With a control inversion, in which the prior flux has the same global annual total flux as
5 the true flux, but has different seasonal and diurnal cycle, we assessed the consequence of
6 ACOS-GOSAT spatiotemporally biased sampling on the estimated annual flux in both
7 the global and regional scale when using a diagonal prior flux error covariance. ACOS-
8 GOSAT observations sample the atmosphere during daytime and have dense observation
9 coverage during boreal summer, so the mean X_{CO_2} sampled at ACOS-GOSAT observing
10 locations and times has lower value than the mean X_{CO_2} sampled everywhere. Even
11 forced by the same annual total fluxes, the global annual mean X_{CO_2} from the nature run
12 is about 0.37 ppm lower than the X_{CO_2} forced by the prior flux when sampled at the
13 ACOS-GOSAT locations and times. This leads to ~ 0.7 GtC more sink in the posterior
14 global flux than the true flux when neglecting the temporal correlation in the prior flux
15 error covariance. Because of the seasonally dependent sampling over the NH boreal
16 region (e.g., Europe) and the stronger seasonal and diurnal cycle of the true flux, the
17 posterior annual total flux over the NH boreal region also has a larger sink than the true
18 flux. Previous studies (Corbin and Denning, 2006; Corbin et al., 2008; Parazoo et al.,
19 2012) show that clear-sky and daytime only sampling introduces bias in the satellite X_{CO_2}
20 observations. The seasonally dependent sampling has not been quantitatively discussed
21 before. In most of the previous OSSE studies (e.g., Baker et al., 2010; Chevallier et al.,
22 2010b), they assume no diurnal cycle in the prior flux (Baker et al., 2010) or assume the
23 same diurnal and seasonal cycles in both the prior and the true fluxes (Chevallier et al.,

1 2010b). The current state-of-the-art inversion systems (e.g., Chevallier et al., 2007; Baker
2 et al., 2010; Basu et al., 2013) do not have seasonal temporal correlation in the prior flux
3 error covariance matrix, though some inversion systems (e.g., Chevallier et al., 2010b;
4 Yadav and Michalak, 2013) include temporal error correlations that decay exponentially
5 with time. However, the prior fluxes used in inversions most likely have different
6 seasonal cycle and diurnal cycle from reality. Yang et al. (2007) and Keppel-Aleks
7 (2012) both find that the seasonal cycle of CASA climatology flux, which is widely used
8 in flux inversions, is about 30% to 40% weaker than the seasonal cycle constrained by
9 X_{CO_2} . Therefore, caution is needed to interpret the global and regional annual net flux
10 estimated from spatiotemporally biased sampling observations, such as GOSAT.

11

12 This study demonstrates the significant impact on flux estimation of assimilating
13 simulated ACOS-GOSAT observations with the CMS flux inversion system. However,
14 the CMS flux inversion system has some common problems with other inversion
15 systems, and these problems require more investigation. These problems include, but are
16 not limited to, the specification of prior flux error statistics, uncertainty quantification,
17 and the impact of transport errors.

18

19 **Appendix A**

20 **Validation of GEOS-Chem CO₂ adjoint model**

21 The validation method for the CO₂ adjoint model is similar to the GEOS-Chem full
22 chemistry adjoint model (Henze et al., 2007). The adjoint code for the CO₂ emissions and
23 vertical transport processes is validated by comparing sensitivities calculated with the

1 adjoint model to sensitivities calculated using finite differences. For this comparison,
2 horizontal transport is turned off in both the forward and adjoint model (advection is
3 discussed in more depth below), rendering the GEOS-Chem model an ensemble of
4 column models. We then calculate the sensitivity of CO₂ concentrations at the surface of
5 one column with respect to scaling factors applied to initial conditions in that column one
6 month earlier. In this configuration, both finite difference and adjoint sensitivities can be
7 evaluated simultaneously throughout the model domain. This is preferable to validating
8 the adjoint model with horizontal transport included, in which case either thousands of
9 model runs are required to have a set of comparable sensitivities, or the comparison is
10 limited to a small number of arbitrarily selected locations. The slope and regression
11 coefficients (r^2) comparing the sensitivities evaluated using adjoint versus finite
12 difference calculations in each model column throughout the globe are 0.999 and 0.999
13 respectively, which confirms the accuracy of the adjoint code. Similar tests were
14 performed to validate that the adjoint sensitivities with respect to the emissions scaling
15 factors are also calculated correctly.

16

17 The adjoint of the horizontal advection operator in GEOS-Chem is solved using the
18 continuous approach, wherein the sign of the winds is reversed and the same numerical
19 solver (the 2nd order piecewise parabolic solver of Lin and Rood (1996)) is used in the
20 solution of the adjoint advection equation as is used in the forward GEOS-Chem model,
21 and the evolution of the model's pressure field is backtracked following the forward
22 model (i.e., the continuity equation is kept as a hard constraint to enforce consistency
23 between the forward and adjoint transport). The details were described in Henze et al.

1 (2007), as well several other studies (Vukicevic et al., 2001; Thuburn and Haine, 2001;
2 Hakami et al., 2007; Gou and Sandu, 2011).

3 **Acknowledgement**

4 We acknowledge the funding support from NASA Carbon Monitoring System program,
5 NASA ACOS CO₂ project (D. K. Henze), and OCO-2 science team grant (11-OCO211-
6 24). We would like to thank four anonymous reviewers for their constructive comments.

7 The GOSAT-ACOS X_{CO₂} data were produced by the ACOS/OCO-2 project at the Jet
8 Propulsion Laboratory, California Institute of Technology, and obtained from the
9 ACOS/OCO-2 data archive maintained at the NASA Goddard Earth Science Data and
10 Information Services Center. The GOSAT spectra were provided to the ACOS Team
11 through a GOSAT Research Announcement (RA) agreement between the California
12 Institute of Technology and the three parties, JAXA, NIES and the MOE. A portion of
13 this research was carried out at the Jet Propulsion Laboratory, California Institute of
14 Technology, under a contract with the National Aeronautics and Space Administration.

15 **References**

- 16 Andres, R. J., Gregg, J. S., Losey, L., Marland, G., and Boden, T. A. 2011. Monthly,
17 global emissions of carbon dioxide from fossil fuel consumption, *Tellus* 63B (3),
18 doi:10.1111/j.1600-0889.2011.00530.x.
- 19 Baker, D. F., Bösch, H., Doney, S. C., O'Brien, D., and Schimel, D. S. 2010. Carbon
20 source/sink information provided by column CO₂ measurements from the Orbiting
21 Carbon Observatory, *Atmos. Chem. Phys.*, 10, 4145–4165, doi:10.5194/acp-10-4145-
22 2010.

1 Basu, S., Guerlet, S., Butz, A., Houweling, S., Hasekamp, O., Aben, I., Krummel, P.,
2 Steele, P., Langenfelds, R., Torn, M., Biraud, S., Stephens, B., Andrews, A., and
3 Worthy, D. 2013. Global CO₂ fluxes estimated from GOSAT retrievals of total
4 column CO₂, *Atmos. Chem. Phys.*, 13, 8695–8717, doi:10.5194/acp-13-8695-2013.

5 Bowman, K., and Henze, D. K. 2012. Attribution of direct ozone radiative forcing to
6 spatially resolved emissions, *Geophys. Res. Lett.*, 39, L22704,
7 doi:10.1029/2012GL053274.

8 Byrd, R. H., Nocedal, J., Schnabel, R. B. 1994. Representations of Quasi-Newton
9 Matrices and their use in Limited Memory Methods. *Mathematical Programming* , 63
10 (4), 129–156. doi:10.1007/BF01582063.

11 Chevallier, F., Peylin, P., Bousquet, S. S. P., Bre´on, F.-M., Che´din, A., and Ciais, P.
12 2005. Inferring CO₂ sources and sinks from satellite observations: Method and
13 application to TOVS data, *J. Geophys. Res.*, 110, D24309,
14 doi:10.1029/2005JD006390.

15 Chevallier, F., Bre´on, F.-M., and Rayner, P. J. 2007. Contribution of the Orbiting Carbon
16 Observatory to the estimation of CO₂ sources and sinks: Theoretical study in a
17 variational data assimilation framework, *J. Geophys. Res.*, 112, D09307,
18 doi:10.1029/2006JD007375.

19 Chevallier, F., Maksyutov, S., Bousquet, P., Breon, F.-M., Saito, R., Yoshida, Y., and
20 Yokota, T. 2009. On the accuracy of the CO₂ surface fluxes to be estimated from the
21 GOSAT observations. *Geophys. Res. Lett.*, 36, L19807, doi:10.1029/2009GL040108.

1 Chevallier, F., Feng, L., Bosch, H., Palmer, P. I., and Rayner, P. J. 2010b. On the impact
2 of transport model errors for the estimation of surface fluxes from GOSAT
3 observations, *Geophys. Res. Lett.*, 37, L21803, doi:10.1029/2010GL044652.

4 Chevallier, F., Wang, T., Ciais, P., Maignan, F., Bocquet, M. and co-authors. 2012. What
5 eddy-covariance measurements tell us about prior land flux errors in CO₂-flux
6 inversion schemes, *Global Biogeochem. Cy.*, 26, GB1021,
7 doi:10.1029/2010GB003974.

8 Corbin, K. D., Denning, A. S. 2006. Using continuous data to estimate clear-sky errors in
9 inversions of satellite CO₂ measurements, *Geophys. Res. Lett.*, 33, L12810,
10 doi:10.1029/2006GL025910.

11 Corbin, K. D., Denning, A. S., Lu, L., Wang, J.-W., and Baker, I. T. 2008. Possible
12 representation errors in inversions of satellite CO₂ retrievals. *J. Geophys. Res.*, 113,
13 D02301, doi:10.1029/2007JD008716

14 Cox, P. M., Betts, R. A., Jones, C. D., Spall, S. A., and Totterdell, I. J. 2000. Acceleration
15 of global warming due to carbon-cycle feedbacks in a coupled climate model. *Nature*,
16 408, 184–187.

17 Crisp, D., Miller, C. E., and DeCola, P. L. 2008. NASA Orbiting Carbon Observatory:
18 measuring the column averaged carbon dioxide mole fraction from space, *J. Appl.*
19 *Remote Sens.*, 2. 023508, doi:10.1117/1.2898457.

20 Crisp, D., Fisher, B. M., O'Dell, C., Frankenberg, C., Basilio, R., Bösch, H.,
21 Brown, L. R., Castano, R., Connor, B., Deutscher, N. M., Eldering, A., Griffith, D.,
22 Gunson, M., Kuze, A., Mandrake, L., McDuffie, J., Messerschmidt, J., Miller, C. E.,
23 Morino, I., Natraj, V., Notholt, J., O'Brien, D. M., Oyafuso, F., Polonsky, I.,

1 Robinson, J., Salawitch, R., Sherlock, V., Smyth, M., Suto, H., Taylor, T. E.,
2 Thompson, D. R., Wennberg, P. O., Wunch, D., and Yung, Y. L. 2012. The ACOS
3 CO₂ retrieval algorithm – Part II: Global X_{CO₂} data characterization, *Atmos. Meas.*
4 *Tech.*, 5, 687-707, doi:10.5194/amt-5-687-2012.

5 Dutkiewicz, S., Follows, M. J., and Bragg, J. G. 2009. Modeling the coupling of ocean
6 ecology and biogeochemistry, *Global Biogeochemical Cycles*, 23, GB4017,
7 doi:10.1029/2008GB003405.

8 Follows, M. J., Dutkiewicz, S., Grant, S., and Chisholm, S. W. 2007. Emergent
9 biogeography of microbial communities in a model ocean, *Science*, 315, 1843–1846,
10 doi:10.1126/science.1138544.

11 Follows, M. J. and Dutkiewicz S. 2011. Modeling diverse communities of marine
12 microbes, *Annual Review of Marine Science*, 3(1), 427–451, doi:10.1146/annurev-
13 marine-120709-142848.

14 Friedlingstein, P., Cox, P., Betts, R. A., Bopp, L., von Bloh, W., Brovkin, V., Cadule, P.,
15 Doney, S., Eby, M., Fung, I., Bala, G., John, J., Jones, C., Joos, F., Kato, T.,
16 Kawamiya, M., Knorr, W., Lindsay, K., Matthews, H.D., Raddatz, T., Rayner, P.,
17 Reick, C., Roeckner, E., Schnitzler, K.G., Schnur, R., Strassmann, K., Weaver, A.J.,
18 Yoshikawa, C., and Zeng, N. 2006. Climate–Carbon Cycle Feedback Analysis:
19 Results from the C4MIP Model Intercomparison. *J. Climate*, 19, 3337–3353.

20 Gloor, M., Sarmiento, J. L., and Gruber, N. 2010. What can be learned about carbon
21 cycle climate feedbacks from the CO₂ airborne fraction?, *Atmos. Chem. Phys.*, 10,
22 7739–7751, doi:10.5194/acp-10-7739-2010.

23 Gruber, N., Gloor, M., Fletcher, S. E. M., Doney, S. C., Dutkiewicz, S., Follows, M. J.,

1 Gerber, M., Jacobson, A. R., Joos, F., Lind- say, K., Menemenlis, D., Mouchet, A.,
2 Mu ÷ller, S. A., Sarmiento, J. L., and Takahashi, T. 2009. Oceanic sources, sinks, and
3 transport of atmospheric CO₂, *Global Biogeochem. Cy.*, 23, GB1005,
4 doi:10.1029/2008GB003349.

5 Gurney, K. R., Law, R. M., Denning, A. S., Rayner, P. J., Baker, D. and co-authors.
6 2003. TransCom 3 CO₂ inversion intercomparison: 1. Annual mean control results
7 and sensitivity to transport and prior flux information, *Tellus B*, 55(2), 555–579,
8 2003.

9 Gou, T. Y. and Sandu, A. 2011. Continuous versus discrete advection adjoints in
10 chemical data assimilation with CMAQ. *Atmospheric Environment*, 45, 4868-4881.

11 Hakami, A., Henze, D. K., Seinfeld, J. H., Singh, K., Sandu, A., Kim, S., Byun, D., and
12 Li, Q. 2007. The adjoint of {CMAQ}. *Environmental Science and Technology*, 41,
13 7807–7817.

14 Henze, D. K., Hakami, A., and Seinfeld, J. H. 2007. Development of the adjoint of
15 GEOS-Chem, *Atmos. Chem. Phys.*, 7, 2413–2433, 2007, [http://www.atmos-chem-](http://www.atmos-chem-phys.net/7/2413/2007/)
16 [phys.net/7/2413/2007/](http://www.atmos-chem-phys.net/7/2413/2007/).

17 Henze, D. K., Seinfeld, J. H., and Shindell, D. T. 2009. Inverse modeling and mapping
18 US air quality influences of inorganic PM_{2.5} precursor emissions using the adjoint of
19 GEOS-Chem, *Atmos. Chem. Phys.*, 9, 5877-5903, doi:10.5194/acp-9-5877-2009.

20 Kalnay, E. 2003. *Atmospheric modeling, data assimilation and pre-dictability*, Cambridge
21 University Press, UK.

22 Keppel-Aleks, G., Wennberg, P. O., and Schneider, T. 2011. Sources of variations in
23 total column carbon dioxide, *Atmos. Chem. Phys.*, 11, 3581-3593, doi:10.5194/acp-

1 11-3581–2011.

2 Keppel-Aleks, G., Wennberg, P. O., Washenfelder, R. A., Wunch, D., Schneider, T.,
3 Toon, G. C., Andres, R. J., Blavier, J.-F., Connor, B., Davis, K. J., Desai, A. R.,
4 Messerschmidt, J., Notholt, J., Roehl, C. M., Sherlock, V., Stephens, B. B., Vay, S. A.,
5 and Wofsy, S. C. 2012. The imprint of surface fluxes and transport on variations in
6 total column carbon dioxide, *Biogeosciences*, 9, 875-891, doi:10.5194/bg-9-875-2012.

7 Kopacz, M., Jacob, D. J., Henze, D. K., Heald, C. L., Streets, D. G., and Zhang, Q. 2009.
8 Comparison of adjoint and analytical Bayesian inversion methods for constraining
9 Asian sources of carbon monoxide using satellite (MOPITT) measurements of CO
10 columns, *J. Geophys. Res.*, 114, D04305, doi:10.1029/2007JD009264.

11 Kopacz, M., Jacob, D. J., Fisher, J. A., Logan, J. A., Zhang, L., Megretskaja, I. A.,
12 Yantosca, R. M., Singh, K., Henze, D. K., Burrows, J. P., Buchwitz, M.,
13 Khlystova, I., McMillan, W. W., Gille, J. C., Edwards, D. P., Eldering, A.,
14 Thouret, V., and Nedelec, P. 2010. Global estimates of CO sources with high
15 resolution by adjoint inversion of multiple satellite datasets (MOPITT, AIRS,
16 SCIAMACHY, TES), *Atmos. Chem. Phys.*, 10, 855–876, doi:10.5194/acp-10-855-
17 2010.

18 Lepers E, Lambin, E. F., Janetos A. C., Defries, R., Achard, F. and co-authors. 2005. A
19 synthesis of information on rapid land-cover change for the period 1981–2000.
20 *BioScience*, 55, 115–124.

21 Le Qu´er´e, C., Andres, R. J., Boden, T., Conway, T., Houghton, R. A. and co-authors,
22 2013, 2013, The global carbon budget 1959–2011, *Earth System Science Data*, 5(1),
23 165–185, doi:10.5194/essd-5-165-2013.

1 Lin, S. J. and Rood, R. B. 1996. Multidimensional flux-form semi-Lagrangian transport
2 schemes. *Monthly Weather Review*, 124, 2046–2070.

3 Los, S. O., Collatz, G. J., Sellers, P. J., Malmstrom, C. M., Pollack, N. H., DeFries, R. S.,
4 Bounoua, L., Parris, M. T., Tucker, C. J., and Dazlich, D. A. 2000. A global 9-yr
5 biophysical land surface dataset from NOAA AVHRR data, *J. Hydrometeorol.*, 1,
6 183–199.

7 Mann, M. E., Bradley, R. S., and Hughes, M. K. 1998. Global-scale temperature patterns
8 and climate forcing over the past six centuries, *Nature*, 392, 779–787.

9 Marshall, J., Adcroft, A., Hill, C., Perelman, L., and Heisey, C. 1997a. A finite-volume,
10 incompressible navier stokes model for studies of the ocean on parallel computers, *J.*
11 *Geophys. Res.-Atmos.*, 102(C3), 5753–5766, doi:10.1029/96JC02775.

12 Marshall, J., Hill, C., Perelman, L., and Adcroft, A. 1997b. Hydrostatic, quasi-
13 hydrostatic, and nonhydrostatic ocean modeling, *J. Geophys. Res.*, 102(C3), 5733–
14 5752, doi:10.1029/96JC02776.

15 Menemenlis, D., Hill, C., Adcroft, A., Campin, J.-M., Cheng, B. and co-authors. 2005.
16 NASA supercomputer improves prospects for ocean climate research, *EOS*, 86(9), 89,
17 96, doi:10.1029/2005EO090002.

18 Menemenlis, D., Campin, J., Heimbach, P., Hill, C., Lee, T., Nguyen, A., Schodlock, M.,
19 and Zhang, H. 2008. ECCO2: High resolution global ocean and sea ice data
20 synthesis, *Mercator Ocean Quarterly Newsletter*, 31, 13–21.

21 Michalak, A. M., Hirsch, A., Bruhwiler, L., Gurney, K. R., Peters, W., and Tans, P. P.
22 2005. Maximum likelihood estimation of covariance parameters for Bayesian
23 atmospheric trace gas surface flux inversions, *J. Geophys. Res.*, 110, D24107,

1 doi:10.1029/2005JD005970.

2 Miller, C. E., Crisp, D., Decola, P. L., Olsen, S. C., Randerson, J. T. and co-authors.

3 2007. Precision requirements for space-based X_{CO2} data, *J. Geophys. Res.*, 112,

4 D10314, doi:10.1029/2006JD007659.

5 Mu, M., J.T. Randerson, G.R. van der Werf, L. Giglio, P. Kasibhatla, D. Morton, G.J.

6 Collatz, R.S. DeFries, E.J. Hyer, E.M. Prins, D.W.T. Griffith, D. Wunch, G.C. Toon,

7 V. Sherlock, and P.O. Wennberg. 2010. Daily and 3-hourly variability in global fire

8 emissions and consequences for atmospheric model predictions of carbon monoxide.

9 *J. Geophys. Res.*, 116: D24303. doi:10.1029/2011JD016245.

10 Nassar, R., Jones, D. B. A., Suntharalingam, P., Chen, J. M., Andres, R. J., Wecht, K. J.,

11 Yantosca, R. M., Kulawik, S. S., Bowman, K. W., Worden, J. R., Machida, T., and

12 Matsueda, H. 2010. Modeling global atmospheric CO₂ with improved emission

13 inventories and CO₂ production from the oxidation of other carbon species, *Geosci.*

14 *Model Dev.*, 3, 689-716, doi:10.5194/gmd-3-689-2010.

15 Nassar, R., Jones, D. B. A., Kulawik, S. S., Worden, J. R., Bowman, K. W., Andres, R. J.,

16 Suntharalingam, P., Chen, J. M., Brenninkmeijer, C. A. M., Schuck, T. J.,

17 Conway, T. J., and Worthy, D. E. 2011. Inverse modeling of CO₂ sources and sinks

18 using satellite observations of CO₂ from TES and surface flask measurements,

19 *Atmos. Chem. Phys.*, 11, 6029-6047, doi:10.5194/acp-11-6029-2011.

20 O'Dell, C. W., Connor, B., Bösch, H., O'Brien, D., Frankenberg, C., Castano, R.,

21 Christi, M., Eldering, D., Fisher, B., Gunson, M., McDuffie, J., Miller, C. E.,

22 Natraj, V., Oyafuso, F., Polonsky, I., Smyth, M., Taylor, T., Toon, G. C.,

23 Wennberg, P. O., and Wunch, D. 2012. The ACOS CO₂ retrieval algorithm – Part 1:

1 Description and validation against synthetic observations, *Atmos. Meas. Tech.*, 5, 99–
2 121, doi:10.5194/amt-5-99-2012.

3 Olsen, S. C. and Randerson, J. T. 2004. Differences between sur- face and column
4 atmospheric CO₂ and implications for carbon cycle research, *J. Geophys. Res.*, 109,
5 D02301, doi:10.1029/2003JD003968.

6 Parazoo, N. C., Denning, A. S., Kawa, S. R., Pawson, S., and Lokupitiya, R. 2012. CO₂
7 flux estimation errors associated with moist atmospheric processes, *Atmos. Chem.*
8 *Phys.*, 12, 6405-6416, doi:10.5194/acp-12-6405-2012, 2012.

9 Parazoo, N., Bowman, K., Frankenberg, C., Lee, J.-E., Fisher, J. B. and co-authors.
10 2013. Interpreting Seasonal Changes in the Carbon Balance of Southern Amazonia
11 Using Measurements of XCO₂ and Chlorophyll Fluorescence from GOSAT. *Geophys.*
12 *Res. Lett.*, DOI: 10.1002/grl.50452.

13 Randerson, J. T., Thompson, M. V., Conway, T. J., Fung, I. Y., and Field, C. S. 1997.
14 The contribution of terrestrial sources and sinks to trends in the seasonal cycle of
15 atmospheric carbon dioxide, *Global Biogeochem. Cy.*, **11**, 535–560.

16 Rienecker, M. M., Suarez, M. J., Todling, R., Bacmeister, J., Takacs, L. and co-authors.
17 2008. The GEOS-5 Data Assimilation System-Documentation of versions 5.0.1 and
18 5.1.0, and 5.2.0 NASA Tech. Rep. Series on Global Modeling and Data Assimilation,
19 NASA/TM-2008-104606, Vol. 27, 92pp.

20 Rienecker, M. M., Suarez, M. J., Gelaro, R., Todling, R., Bacmeister, J. and co-authors.
21 2011. MERRA: NASA’s Modern-Era Retrospective Analysis for Research and
22 Applications. *J. Climate*, 24, 3624–3648.

1 Rodgers, C. D. 2000. Inverse Methods for Atmospheric Sounding: Theory and Practice,
2 238 pp., World Sci., Hackensack, NJ.

3 Sarmiento, J. L., Gloor, M., Gruber, N., Beaulieu, C., Jacobson, A. R.,
4 Mikaloff Fletcher, S. E., Pacala, S., and Rodgers, K. 2010. Trends and regional
5 distributions of land and ocean carbon sinks, *Biogeosciences*, 7, 2351–2367,
6 doi:10.5194/bg-7-2351-2010.

7 Stephens, B. B., Gurney, K. R., Tans, P. P., Sweeney, C., Peters, W., Bruhwiler, L.,
8 Ciais, P., Ramonet, M., Bousquet, P., Nakazawa, T. and co-authors. 2007. Weak
9 northern and strong tropical land carbon uptake from vertical profiles of atmospheric
10 CO₂, *Science*, 316, 1732–1735.

11 Suntharalingam, P., Jacob, D. J., Palmer, P. I., Logan, J. A., Yantosca, R. M., Xiao, Y.,
12 Evans, M. J., Streets, D. G., Vay, S. L., Sachse, G. W. 2004. Improved
13 quantification of Chinese carbon fluxes using CO₂/CO correlations in Asian outflow,
14 *J. Geophys. Res.*, 109, D18S18, doi:10.1029/2003JD004362.

15 Takahashi, T., Sutherland, S. C., Sweeney, C., Poisson, A., Metzl, N., Tillbrook, B.,
16 Bates, N., Wanninkhof, R., Feely, R. A., Sabine, C., Olafsson, J. and Nojiri, Y. 2002.
17 Global sea-air CO₂ flux based on climatological surface ocean pCO₂, and seasonal
18 biological and temperature effects, *Deep-Sea Res. II*, 49, 1601–1622.

19 Tarantola, A. 2005. Inverse Problem Theory: Methods for Data Fitting and Model
20 Parameter Estimation, Society for Industrial and Applied Mathematics (SIAM).

21 Thuburn, J. and Haine, T. W. N. 2001. Adjoint of nonoscillatory advection schemes.
22 *Journal of Computational Physics*, 171, 616–631.

1 Tucker C. J., Pinzon, J. E., Brown, M. E., Slayback, D. A., Pak, E. W., Mahoney, R.,
2 Vermote, E. F., El Saleous, N. 2005. An extended AVHRR 8-km NDVI data set
3 compatible with MODIS and SPOT vegetation NDVI data, *Int. J. Remote Sens.*,
4 26, 4485–4498.

5 van der Werf, G. R., Randerson, J. T., Collatz, G. J., Giglio, L., Kasibhatla, P. S.,
6 Arellano, A. F., Olsen, S. C., and Kasischke, E. S. 2004. Continental-scale
7 partitioning of fire emissions during the 1997 to 2001 El Niño/La Niña period,
8 *Science*, 303, 73–76.

9 van der Werf, G. R., Randerson, J. T., Giglio, L., Collatz, G. J., Kasibhatla, P. S., and
10 Arellano Jr., A. F. 2006. Interannual variability in global biomass burning emissions
11 from 1997 to 2004, *Atmos. Chem. Phys.*, 6, 3423–3441, doi:10.5194/acp-6-3423-
12 2006.

13 van der Werf, G. R., Randerson, J. T., Giglio, L., Collatz, G. J., Mu, M., Kasibhatla, P.
14 S., Morton, D. C., DeFries, R. S., Jin, Y., and van Leeuwen, T. T. 2010. Global fire
15 emissions and the contribution of deforestation, savanna, forest, agricultural, and peat
16 fires (1997–2009), *Atmos. Chem. Phys.*, 10, 11707–11735, doi:10.5194/acp-10-
17 11707-2010.

18 Vukicevic, T., Steyskal, M., and Hecht, M. 2001. Properties of advection algorithms in
19 the context of variational data assimilation. *Mon. Weather Rev.*, 129, 1221–1231.

20 Wunch, D., Wennberg, P. O., Toon, G. C., Connor, B. J., Fisher, B. and co-authors. 2011.
21 A method for evaluating bias in global measurements of CO₂ total columns from
22 space, *Atmos. Chem. Phys.*, 11, 12317–12337, doi:10.5194/acp-11-12317-2011.

23 Yadav, V. and Michalak, A. M. 2013. Improving computational efficiency in large linear

1 inverse problems: an example from carbon dioxide flux estimation, *Geosci. Model*
2 *Dev.*, 6, 583-590, doi:10.5194/gmd-6-583-2013, 2013.

3 Yang, Z., Washenfelder, R. A., Keppel-Aleks, G., Krakauer, N. Y., Randerson, J. T.,
4 Tans, P. P., Sweeney, C., and Wennberg, P. O. 2007. New constraints on Northern
5 Hemisphere growing season net flux, *Geophys. Res. Lett.*, 34, L12807,
6 doi:10.1029/2007GL029742.

7 Yokota, T., Yoshida, Y., Eguchi, N., Ota, Y., Tanaka, T., Watan-
8 abe, H., and Maksyutov, S. 2009. Global Concentrations of CO₂ and CH₄ Retrieved from
9 GOSAT: First Preliminary Results, *SOLA*, 5, 160–163.

10 Zhu, C., Byrd, R. H., Lu, P.; Nocedal, J. 1997. L-BFGS-B: Algorithm 778: L-BFGS-B,
11 FORTRAN routines for large scale bound constrained optimization, *ACM*
12 *Transactions on Mathematical Software*, 23 (4), 550–560,
13 doi:[10.1145/279232.279236](https://doi.org/10.1145/279232.279236).

14
15
16
17
18
19

1 **Table captions**

2

3 Table 1 List of the carbon budgets and sources for each category of the fluxes (unit:
4 GtC/year)

5

6 **Figure captions**

7 **Figure 1** The annual mean true flux (a), the prior flux (b), and the posterior flux (c) from
8 the control inversion; the zonal mean monthly flux for the truth (d), the prior flux (e), and
9 the posterior flux (f); RMS error of the monthly zonal mean flux for the prior (blue) and
10 the posterior flux (g). (Unit: gC/m²/day)

11

12 **Figure 2** a) Total number of ACOS-GOSAT b2.9 good-quality observations at each 4° x
13 5° grid point during 2010; b) Total number of daily ACOS-GOSAT b2.9 observations at
14 each latitude as a function of time.

15

16 **Figure 3** a) The annual mean prior flux uncertainty (unit: gC/m²/day) calculated from the
17 monthly flux scale factor error statistics used in the inversion; b) the monthly zonal mean
18 prior flux uncertainty (unit: gC/m²/day).

19

20 **Figure 4** a. Global CO₂ flux seasonal cycle (black: the truth; blue: the prior flux; red: the
21 posterior flux assimilating ACOS-GOSAT X_{CO2}; green: the posterior flux assimilating
22 random-sampled X_{CO2}. Unit: GtC/month). b. Global total flux uncertainty reduction as a
23 function of month.

24

25 **Figure 5** a. Comparison of X_{CO2} (unit: ppm) from nature run sampled with different
26 sampling strategies. Blue: daily averaged X_{CO2} sampled at every grid point every three

1 hours; red: daily averaged X_{CO_2} sampled at the ACOS-GOSAT locations every three
2 hours; black: X_{CO_2} sampled at the ACOS-GOSAT locations and observing time. b. Red:
3 the difference between X_{CO_2} sampled at the ACOS-GOSAT locations and the X_{CO_2}
4 sampled everywhere; black: the difference between X_{CO_2} sampled at the ACOS-GOSAT
5 locations and observing time and the X_{CO_2} sampled everywhere every three hours. c.
6 Black: the difference between the observations and the X_{CO_2} forced by the prior flux used
7 in the control inversion; red: the difference between the observations and the X_{CO_2} forced
8 by the flux with the same diurnal cycle as the true flux but with the same seasonal cycle
9 as the prior flux used in the control inversion.

10

11 Figure 6 Flux seasonal cycle comparison among the truth (black), the prior flux (blue)
12 and the posterior flux (red) at 11 TransCom regions over land; purple line is the total
13 number of simulated ACOS-GOSAT observations at each region as a function of month
14 (unit: 100, right y-axis); a: North American Boreal; b: North American Temperate; c:
15 South American Tropical; d: South American Temperate; e: Northern Africa; f: Southern
16 Africa; g: Eurasian boreal; h: Eurasian temperate; i: Tropical Asia; j: Australia; k:
17 Europe. On the top of each panel lists the RMS error of the prior flux (first number) and
18 the posterior flux (second number). Unit: $gC/m^2/day$. l. the geographic boundaries of the
19 11 regions.

20

21 Figure 7 Monthly mean prior flux uncertainty (a) and the uncertainty reduction at 11
22 TransCom regions over land (b). 1: North American Boreal; 2: North American
23 Temperate; 3: South American Tropical; 4: South American Temperate; 5: Northern

1 Africa; 6: Southern Africa; 7: Eurasian boreal; 8: Eurasian temperate; 9: Tropical Asia;
2 10: Australia; 11: Europe.

3

4 **Figure 8** The time averaged absolute X_{CO_2} difference (unit: ppm) between the control run
5 and a separate simulation where the surface flux is perturbed within the rectangle. The
6 magnitude of this perturbation is equal to the difference between the control and nature
7 run surface flux. a: averaged over June and July; b: averaged over November and
8 December. Total number of simulated ACOS-GOSAT observations at each grid cell for
9 these two time periods. c: June and July; d: November and December.

10

1

2 Table 1 List of the carbon budgets and sources for each category of the fluxes (unit:

3 GtC/year)

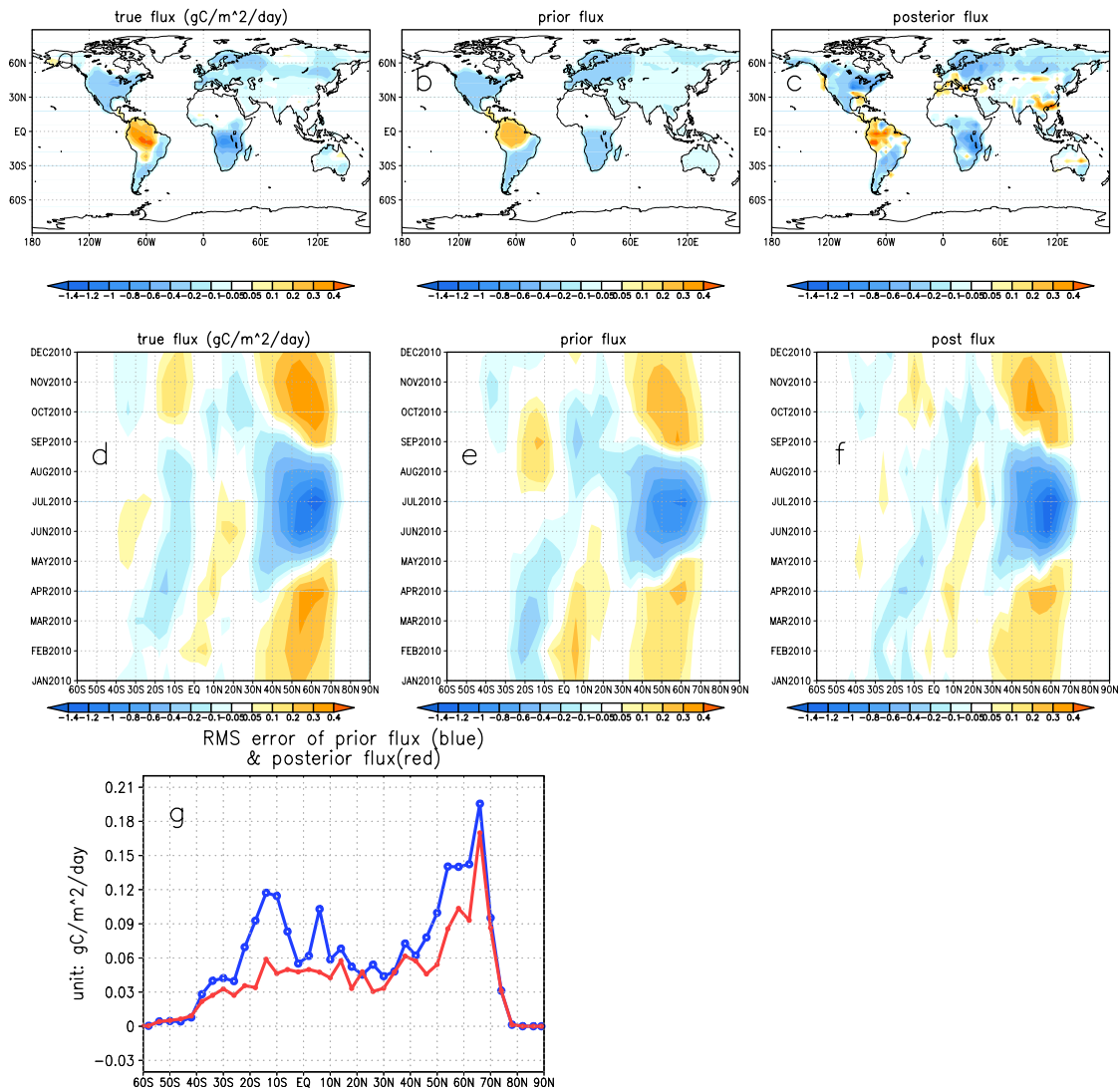
	Fossil fuel	Biomass burning	Shipping + aviation + chemical sources	Ocean flux	Terrestrial Biosphere flux	Total
Sources	CDIAC	GFED3	Nassar et al. (2010)	ECCO2-Darwin	CASA/CASA-GFED3	Net
Carbon Budget	8.1	2.4	2.0	-2.4	-5.3	4.8

4

5

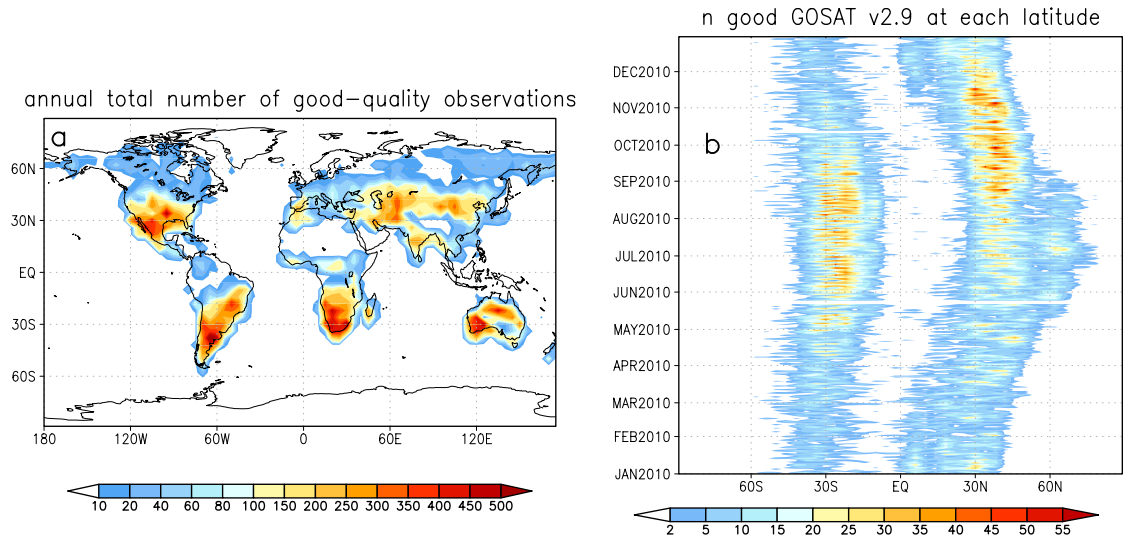
6

1
2



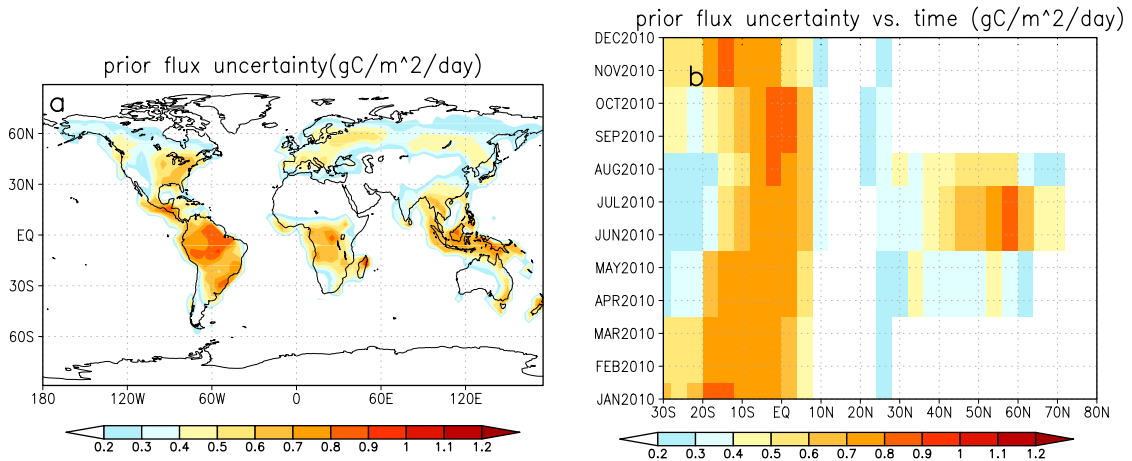
3
4 Figure 1 The annual mean true flux (a), the prior flux (b), and the posterior flux (c) from
5 the control inversion; the zonal mean monthly flux for the truth (d), the prior flux (e), and
6 the posterior flux (f); RMS error of the monthly zonal mean flux for the prior (blue) and
7 the posterior flux (g). (Unit: $\text{gC}/\text{m}^2/\text{day}$)

8
9
10



1
 2 Figure 2 a) Total number of ACOS-GOSAT b2.9 good-quality observations at each 4° x
 3 5° grid point during 2010; b) Total number of daily ACOS-GOSAT b2.9 observations at
 4 each latitude as a function of time.

- 5
- 6
- 7
- 8
- 9
- 10
- 11
- 12
- 13
- 14
- 15
- 16
- 17
- 18
- 19
- 20
- 21
- 22
- 23
- 24



1

2 Figure 3 a) The annual mean prior flux uncertainty (unit: gC/m²/day) calculated from the
 3 monthly flux scale factor error statistics used in the inversion; b) the monthly zonal mean
 4 prior flux uncertainty (unit: gC/m²/day).

5

6

7

8

9

10

11

12

13

14

15

16

17

18

19

20

21

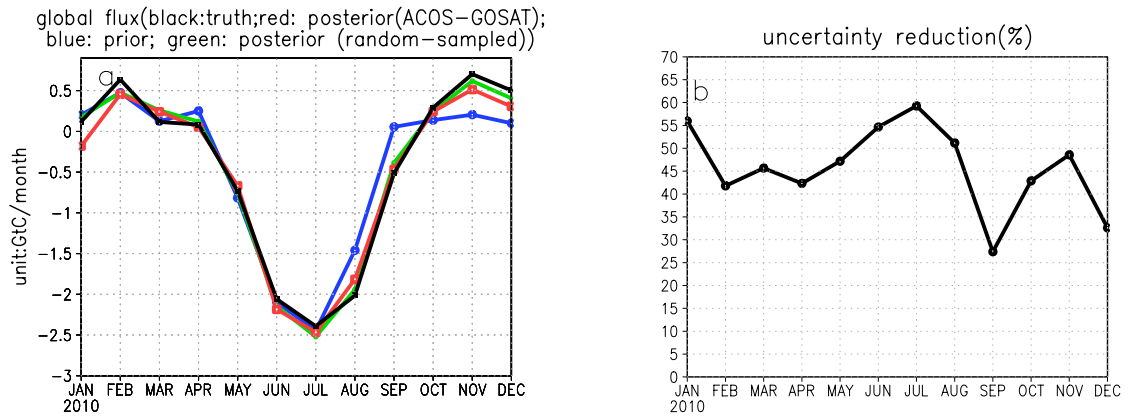
22

23

24

25

1



2

3

4

5

6

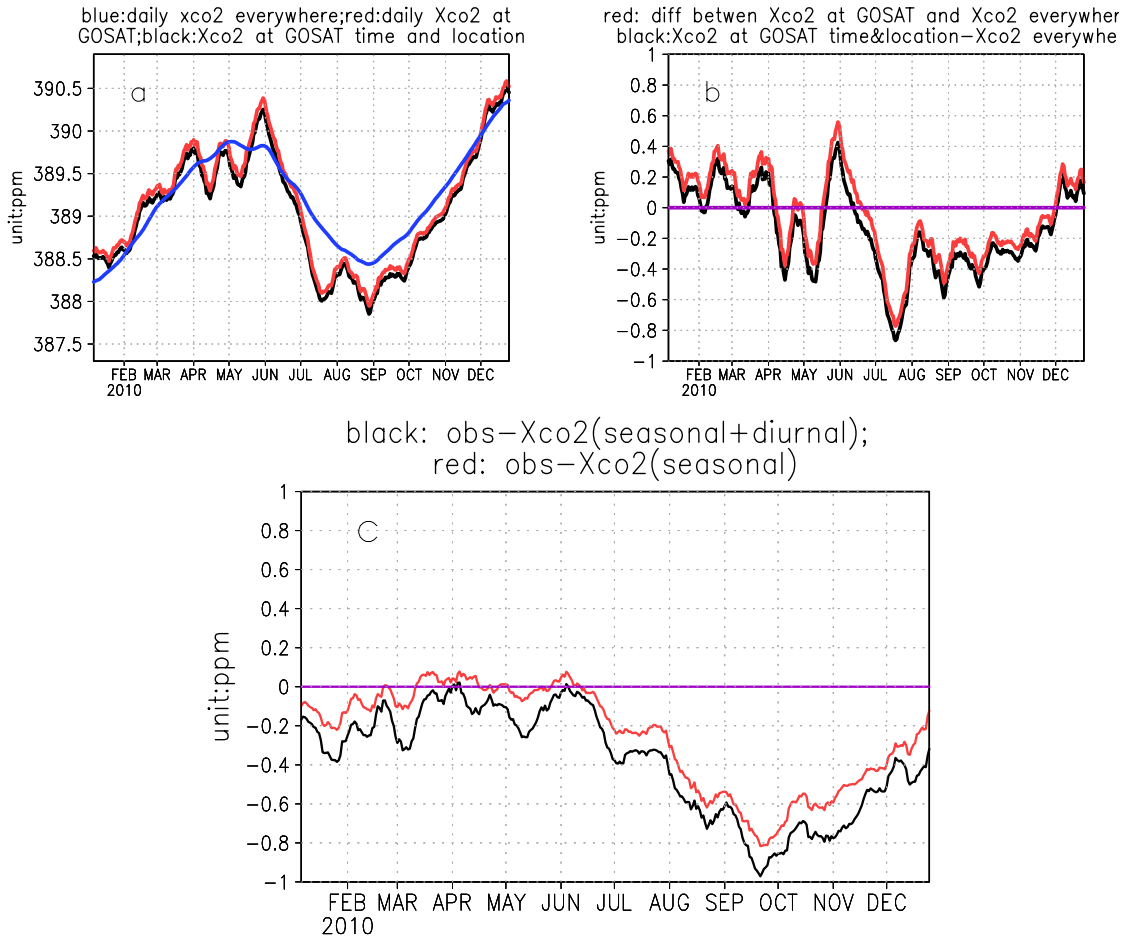
Figure 4 a. Global CO₂ flux seasonal cycle (black: the truth; blue: the prior flux; red: the posterior flux assimilating ACOS-GOSAT X_{CO2}; green: the posterior flux assimilating random-sampled X_{CO2}. Unit: GtC/month). b. Global total flux uncertainty reduction as a function of month.

7

8

9

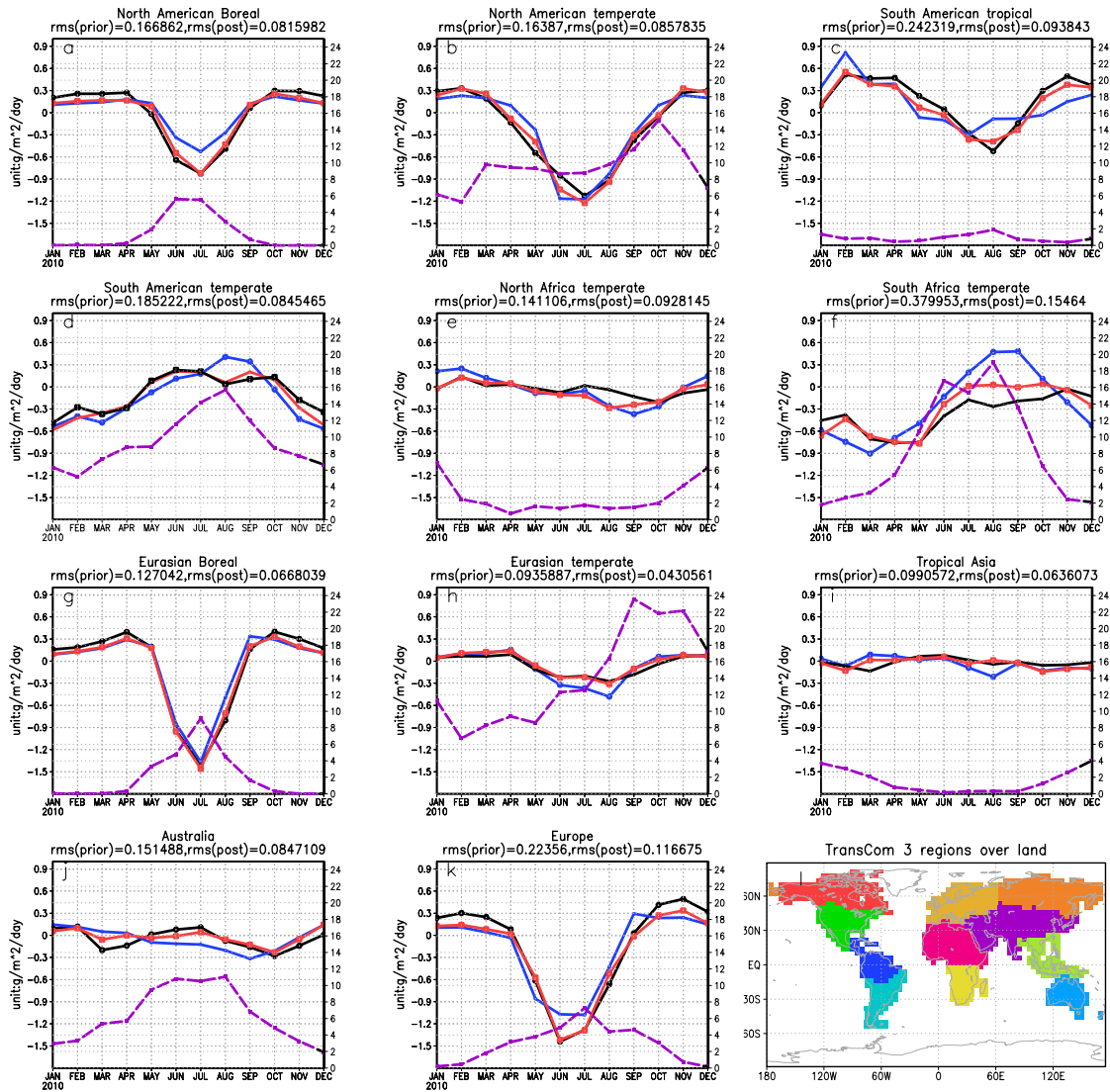
1
2



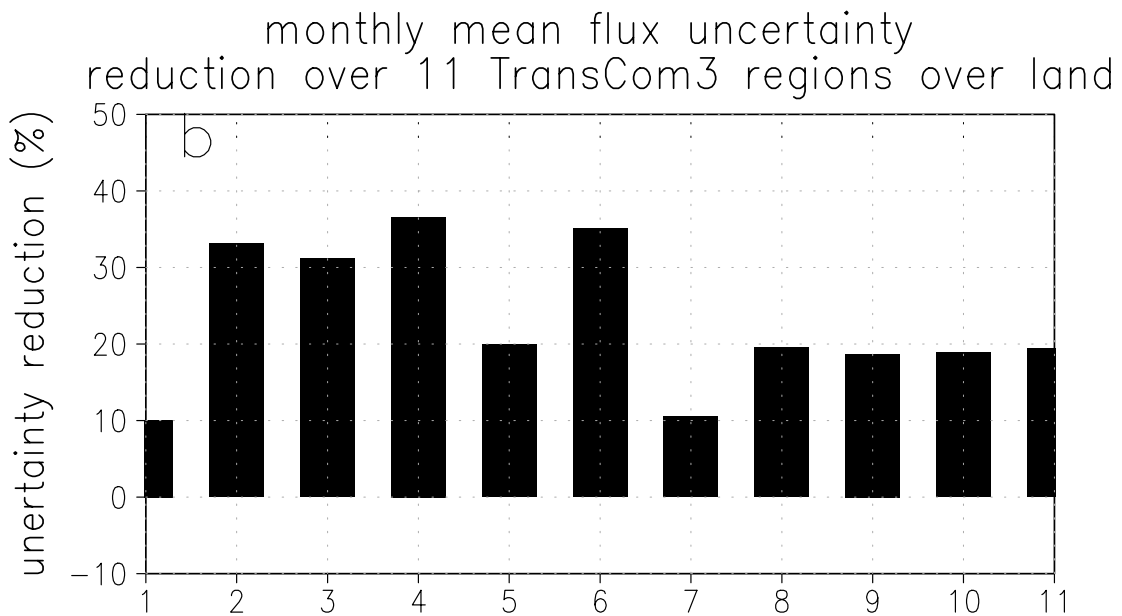
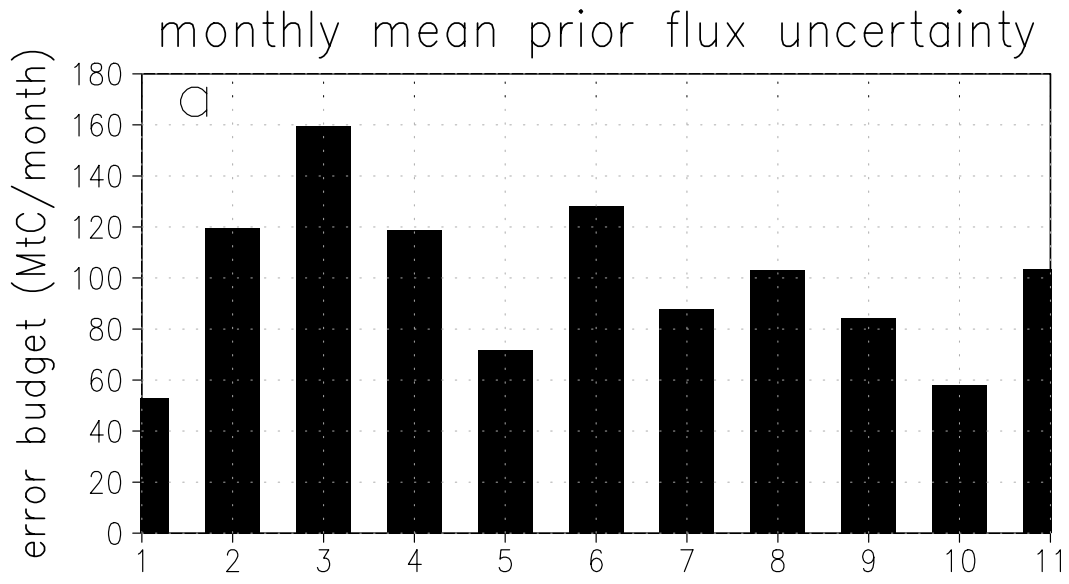
3
4

5 Figure 5 a. Comparison of X_{CO_2} (unit: ppm) from nature run sampled with different
6 sampling strategies. Blue: daily averaged X_{CO_2} sampled at every grid point every three
7 hours; red: daily averaged X_{CO_2} sampled at the ACOS-GOSAT locations every three
8 hours; black: X_{CO_2} sampled at the ACOS-GOSAT locations and observing time. b. Red:
9 the difference between X_{CO_2} sampled at the ACOS-GOSAT locations and the X_{CO_2}
10 sampled everywhere; black: the difference between X_{CO_2} sampled at the ACOS-GOSAT
11 locations and observing time and the X_{CO_2} sampled everywhere every three hours. c.
12 Black: the difference between the observations and the X_{CO_2} forced by the prior flux used
13 in the control inversion; red: the difference between the observations and the X_{CO_2} forced
14 by the flux with the same diurnal cycle as the true flux but with the same seasonal cycle
15 as the prior flux used in the control inversion.

16

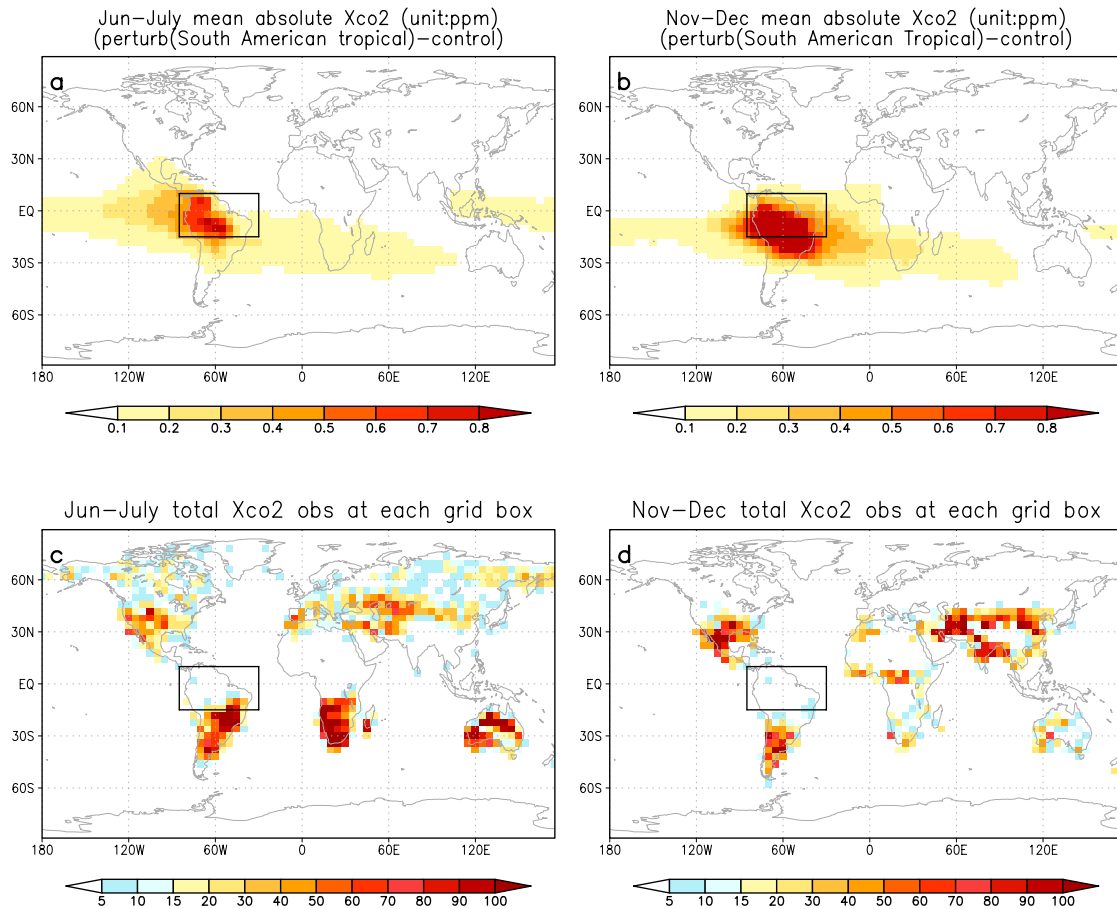


1
 2 Figure 6 Flux seasonal cycle comparison among the truth (black), the prior flux (blue)
 3 and the posterior flux (red) at 11 TransCom regions over land; purple line is the total
 4 number of simulated ACOS-GOSAT observations at each region as a function of month
 5 (unit: 100, right y-axis); a: North American Boreal; b: North American Temperate; c:
 6 South American Tropical; d: South American Temperate; e: Northern Africa; f: Southern
 7 Africa; g: Eurasian boreal; h: Eurasian temperate; i: Tropical Asia; j: Australia; k:
 8 Europe. On the top of each panel lists the RMS error of the prior flux (first number) and
 9 the posterior flux (second number). Unit: gC/m²/day. l. the geographic boundaries of the
 10 11 regions.



1
2

3 Figure 7 Monthly mean prior flux uncertainty (a) and the uncertainty reduction at 11
 4 TransCom regions over land (b). 1: North American Boreal; 2: North American
 5 Temperate; 3: South American Tropical; 4: South American Temperate; 5: Northern
 6 Africa; 6: Southern Africa; 7: Eurasian boreal; 8: Eurasian temperate; 9: Tropical Asia;
 7 10: Australia; 11: Europe.



1
2

3 Figure 8 The time averaged absolute X_{CO2} difference (unit: ppm) between the control run
 4 and a separate simulation where the surface flux is perturbed within the rectangle. The
 5 magnitude of this perturbation is equal to the difference between the control and nature
 6 run surface flux. a: averaged over June and July; b: averaged over November and
 7 December. Total number of simulated ACOS-GOSAT observations at each grid cell for
 8 these two time periods. c: June and July; d: November and December.

9

10

11

12

13